Final Technical Report: Stabilizing the Power System in 2035 and Beyond

Evolving from Grid-Following to Grid-Forming Distributed Inverter Controllers

Yashen Lin,[1] Brian Johnson,[1] Sairaj Dhople,[2] Francesco Bullo,[3] Patrick Chapman,[4] Victor Purba,[2] Saber Jafarpour,[3] Gab-Su Seo,[1] Hugo Villegas-Pico,[1] Nathan Ainsworth,[1] Miguel Rodriguez,[1] Mohammed Khan,[1] Joseph Eto,[5] Abraham Ellis,[6] Jack Flicker,[6] Brian Pierre,[6] and Robert Lasseter[7]

1 National Renewable Energy Laboratory
2 University of Minnesota
3 University of California, Santa Barbara
4 SunPower
5 Lawrence Berkeley National Laboratory
6 Sandia National Laboratories
7 University of Wisconsin

NREL is a national laboratory of the U.S. Department of Energy
Office of Energy Efficiency & Renewable Energy
Operated by the Alliance for Sustainable Energy, LLC

This report is available at no cost from the National Renewable Energy Laboratory (NREL) at www.nrel.gov/publications.

Contract No. DE-AC36-08GO28308

Technical Report
NREL/TP-5D00-79761
August 2021

Final Technical Report: Stabilizing the Power System in 2035 and Beyond

Evolving from Grid-Following to Grid-Forming Distributed Inverter Controllers

Yashen Lin,[1] Brian Johnson,[1] Sairaj Dhople,[2] Francesco Bullo,[3] Patrick Chapman,[4] Victor Purba,[2] Saber Jafarpour,[3] Gab-Su Seo,[1] Hugo Villegas-Pico,[1] Nathan Ainsworth,[1] Miguel Rodriguez,[1] Mohammed Khan,[1] Joseph Eto,[5] Abraham Ellis,[6] Jack Flicker,[6] Brian Pierre,[6] and Robert Lasseter[7]

1 National Renewable Energy Laboratory
2 University of Minnesota
3 University of California, Santa Barbara
4 SunPower
5 Lawrence Berkeley National Laboratory
6 Sandia National Laboratories
7 University of Wisconsin

Suggested Citation
Lin, Yashen, Brian Johnson, Sairaj Dhople, et al. 2021. *Final Technical Report: Stabilizing the Power System in 2035 and Beyond—Evolving from Grid-Following to Grid-Forming Distributed Inverter Controllers*. Golden, CO: National Renewable Energy Laboratory. NREL/TP-5D00-79761. https://www.nrel.gov/docs/fy21osti/79761.pdf.

NREL is a national laboratory of the U.S. Department of Energy
Office of Energy Efficiency & Renewable Energy
Operated by the Alliance for Sustainable Energy, LLC

This report is available at no cost from the National Renewable Energy Laboratory (NREL) at www.nrel.gov/publications.

Contract No. DE-AC36-08GO28308

Technical Report
NREL/TP-5D00-79761
August 2021

National Renewable Energy Laboratory
15013 Denver West Parkway
Golden, CO 80401
303-275-3000 • www.nrel.gov

NOTICE

This work was authored in part by the National Renewable Energy Laboratory, operated by Alliance for Sustainable Energy, LLC, for the U.S. Department of Energy (DOE) under Contract No. DE-AC36-08GO28308. Funding provided by U.S. Department of Energy Office of Energy Efficiency and Renewable Energy Solar Energy Technologies Office Agreement Number 30364. The views expressed herein do not necessarily represent the views of the DOE or the U.S. Government.

Cover Photos by Dennis Schroeder: (clockwise, left to right) NREL 51934, NREL 45897, NREL 42160, NREL 45891, NREL 48097, NREL 46526.

Acknowledgments

This material is based upon work supported by the U.S. Department of Energy's Office of Energy Efficiency and Renewable Energy (EERE) under the SunShot National Laboratory Multiyear Partnership (SuNLaMP) funding program Award Number DE-EE0000-1583.

List of Acronyms

CED	constraint-enforcing droop
DOE	U.S. Department of Energy
dq	direct quadrature
GFL	grid-following
GFM	grid-forming
HIL	hardware-in-the-loop
IEEE	Institute of Electrical and Electronics Engineers
MPPT	maximum power point tracking
NERC	North American Electric Reliability Corporation
NREL	National Renewable Energy Laboratory
omega	frequency
P	real power
PHIL	power-hardware-in-the-loop
PLL	phase-locked loop
PV	photovoltaic
Q	reactive power
V	voltage
VOC	virtual oscillator control

Executive Summary

Under existing grid operations, large synchronous generators provide sufficient rotational inertia to form a rigid backbone for the bulk power system. With photovoltaics (PV) forecasted to provide more than 600 GW of generation by 2050 under the U.S. Department of Energy's SunShot Initiative objectives, however, it is clear that power electronic inverters will play a dominant role in future systems, and low-inertia stability must be ensured to maintain system reliability. Today, the risks to system stability can be observed on geographically small islands, such as Hawaii, which contain a relatively large amount of installed PV. These risks stem from a fundamental shortcoming of contemporary control strategies—existing inverter controllers cannot guarantee grid stability. Given that future power systems driven by sustainable resources will be characterized by low inertia, locations such as Hawaii provide a glimpse into the obstacles facing future power systems. Considering these challenges, the aim of this project was to develop and demonstrate distributed inverter controllers that enable the reliable control of low-inertia power systems with hundreds of gigawatts of integrated PV.

The fundamental challenge in realizing a low-inertia power system is that existing inverter controllers are equipped with grid-following (GFL) controllers. These controllers are built on the assumption that system voltage and frequency are regulated by inertial sources. These prevailing control approaches cannot guarantee system-level stability and are unable to sustain an inverter-dominated infrastructure. The future calls for the deployment of stabilizing grid-forming (GFM) controllers for decentralized inverter networks that actively regulate voltage and frequency.

Focused on these challenges, we leveraged the algorithmic flexibility of digital microcontrollers in designing next-generation inverter controllers for transformative impacts in PV-dominated networks. The new GFM inverter controllers, which we call virtual oscillator control (VOC), are based on the synchronization of networked oscillators. The essence of the proposed method is to digitally control each power electronic inverter to emulate the dynamics of a nonlinear oscillator, where a stable and self-synchronizing power system emerges by design.

The major accomplishments of the project include:

- We developed a comprehensive modeling framework and accompanying case studies for the stability assessment of low-inertia grids with significant penetrations of inverter-based resources. Both the business-as-usual GFL inverter control and the new GFM inverter control were considered. Results show that the system could become unstable as the inverter penetration level increases (as low as 45% in an illustrative single-machine, single-inverter case), and this tipping point depends on several system parameters (such as inverter controller gains and filter parameters). Results also show that GFM inverters can potentially improve the stability of the power system.
- We designed, analyzed, and validated a next-generation, GFM inverter controller—the VOC. We demonstrated that the new controller can regulate inverter output voltage without external voltage reference, share load autonomously among multiple inverters, and is compatible with the existing electric grid. These capabilities are critical to the reliable operation of electric grids and are traditionally provided by large synchronous

generators. Having these capabilities in inverters enables the transition to a future power system that is dominated by inverter-based resources.

- We created a research road map on GFM inverters (Lin et. al. 2020). The project team recognizes that there is no established body of experience for operating hybrid power systems with significant amounts of inverter-based resources at the scale of today's North American interconnections. This road map is intended to provide a comprehensive analysis of the challenges in integrating inverter-based resources and offers recommendations on potential technology pathways to inform the academic community, industry, and government research organizations. The road map also outlines specific research directions appropriate for inclusion in a U.S. national research-and-development program on GFM inverter-based generation and storage that can enhance the stability of future electric power systems.

Table of Contents

List of Figures

List of Tables

1 Background

Managing the stability of today's electric power systems is based on decades of experience with the physical properties and control responses of large synchronous turbine generators. Managing the stability of tomorrow's electric power systems must contend with an increasing proportion of generation from nontraditional sources, such as solar (among others), as well as energy storage devices, such as batteries. In addition to the variable nature of many renewable generation sources (because of the weather-driven nature of their fuel supplies), these newer sources vary in size—from residential-scale rooftop systems (a few kilowatts) to utility-scale power plants (hundreds to even thousands of megawatts)—and they are interconnected throughout the electric grid both from within the distribution system and directly to the high-voltage transmission system. Most important for our purposes, many of these new resources are connected to the power system through power electronic inverters rather than through spinning electromechanical machines.

These differences pose major challenges because the operation of future power systems must be based on a hybrid of the physical properties and control responses of traditional, large synchronous turbine generators as well as those of nontraditional, smaller inverter-based generation sources. Traditionally, synchronous generators maintain the voltage and frequency of the system. They also provide inertia to damp disturbances in the system. Currently, existing inverter-based resources cannot provide these capabilities. Recognizing the generational change, it is important to investigate the stability of coupled inverter-machine systems and to develop next-generation, grid-forming (GFM) inverter controllers to ensure the reliability of future power systems.

1.1 Stability of Coupled Inverter-Machine Systems

Prior work that relates to this effort includes classical results on the stability of interconnected synchronous generators in the bulk system (Bergen and Hill 1981; Kundur, Balu, and Lauby 1994). Given that power electronic energy-conversion interfaces have only recently been deployed in significant numbers and capacities approaching representative values in the bulk system, inverter dynamics have hitherto not been systematically acknowledged. There is a growing body of literature that has investigated the dynamics of (predominantly) inverter-based islanded microgrids (Pogaku, Prodanovic, and Green 2007; Rasheduzzaman, Mueller, and Kimball 2015; Guerrero et al. 2004; Simpson-Porco, Dörfler, and Bullo 2013). Regarding the setting we study, grid-connected inverter systems, destabilizing interactions between inverters with conventional phase-locked loops (PLL) has been recently uncovered and analyzed (Dong et al. 2015); the small-signal stability of mixed inverter-machine microgrids as a function of inverter control gains has been studied (Katiraei, Iravani, and Lehn 2007), and the small-signal stability of a wind turbine-machine system has been investigated (Tan et al. 2012). Although these works have characterized the dynamics of heterogeneous machine-inverter systems to some extent, the effect of inverter penetration level on stability has not been explicitly addressed. Finally, several large-scale system modeling studies have assessed the impact of variable renewable generation on system dynamics (Miller et al. 2015); however, inverters in such studies are typically modeled as real-power injections, and the dynamic models that underly inverter operation are disregarded for analytic and computational convenience.

In this project, we developed a comprehensive modeling framework and accompanying case studies for the stability assessment of low-inertia grids with varying inverter penetration levels. Detailed dynamic models for the inverters and their controller were developed. In the stability analysis, we also proposed model aggregation algorithms to represent a large collection of inverters.

1.2 Grid-Forming Inverters

To address the challenges in low-inertia systems, a variety of GFM strategies have been developed during the past two decades. Existing GFM controllers can be broadly categorized as droop controllers, virtual synchronous machines (often called "synchronverters"), and virtual oscillator controllers (VOC), to name a few. We consider each method as follows.

- *Droop control:* The most well-established GFM method is droop control, which was first proposed in the early 1990s (Chandorkar, Divan, and Adapa 1993). Its key feature is that it exhibits a linear trade-off between frequency and voltage versus real and reactive power, much like a typical synchronous machine does in steady state. These so-called "droop laws" are referred to as the P-omega (real power-frequency) and Q-V (reactive power-voltage) relationships, and they give rise to the following properties regardless of whether they are machines or inverters:
    - System-wide synchronization—all units reach the same frequency.
    - Power sharing—each unit provides power in proportion to its capacity (or its programmable droop slope).

These properties arise as a result of the networked interactions from the grid and locally programmed droop laws.

- *Virtual synchronous machines:* This approach is based on the emulation of a synchronous machine within the controls of an inverter (Beck and Hesse 2007; Alatrash et al. 2012; Zhong 2016). Specifically, inverter terminal measurements are fed as inputs to a digital synchronous machine model whose emulated dynamics are mapped to the inverter output in real time. The complexity of the virtual machine can vary greatly, from detailed electromechanical models to simplified swing dynamics. Implementations that closely match machine characteristics, possibly even with virtual flux dynamics, have both Q-V and P-omega characteristics and are often called "synchronverters." On the other end of the spectrum, virtual inertia methods are simpler and capture only the dynamics of an emulated rotor and its steady-state P-omega droop.
- *VOC:* In recent years, another inverter control method based on the emulation of nonlinear oscillators has emerged (Johnson et al. 2015). Much like a virtual synchronous machine, real-time measurements are processed by the digitally implemented model whose output variables modulate the inverter power stage. As illustrated in Figure 4, the key difference is that the model takes the form of an oscillator circuit with a natural frequency that coincides with the nominal AC grid frequency, and its remaining parameters are tuned to adjust the nominal voltage and control bandwidth. Although the virtual oscillator might appear radically different, it has been shown to exhibit the similar Q-V and P-omega droop laws in steady state.

Despite the differences between droop controllers, virtual synchronous machines, and virtual oscillators, all three methods have similar properties that allow us to consider them as a whole. In particular, the output terminal behavior of an inverter with any of these GFM controllers resembles a voltage source with an amplitude and frequency that varies with reactive power generation and the system load, respectively. This property allows GFM inverters to adjust output power nearly instantaneously to balance loads, regulate local voltage, and contribute to frequency control. Although grid-following (GFL) inverters can be programmed to emulate the GFM properties, they nonetheless require a well-defined terminal voltage as a reference.

Although GFM controllers can be understood by the unifying framework, they exhibit key differences that lead to operational advantages and disadvantages when compared to each other. In particular, the main performance shortcoming in typical GFM controllers is that they exhibit a sluggish response during transients. For instance, a typical droop controller and certain incarnations of inertia/machine emulation could take up to a few seconds to reach steady state after a disturbance. This slow response time can be precisely attributed to significant preprocessing (e.g., low-pass filters and signal delays) of measurements before the controller begins to act. Accordingly, this structure might be too slow for low-inertia systems. Because these controllers are acting on slow-moving, averaged AC quantities that are closely related to the notion of phasors in AC systems, we refer to these strategies as *phasor-based.*

In contrast, VOC is a *time-domain* controller that reacts to instantaneous measurements such that network disturbances are instantly manifested as a response at the inverter controller output. Accordingly, VOC seamlessly integrates with the network physics without any need for signal preprocessing. In addition, note that the steady-state behavior of VOC after a disturbance coincides with the steady-state behavior of droop control. The following observations can be drawn from the results in Sinha et al. (2015a), Sinha et al. (2015b), and Johnson et al. (2015): (1) VOC subsumes the functionality of droop control while acting on a faster timescale, and (2) VOC can be designed such that it is backward compatible with droop control.

2 Project Objectives

The objective of this project is to develop distributed inverter controllers that provide a low-resistance path from the current inertia-dominated grid paradigm to a future grid paradigm dominated by low-inertia power systems with hundreds of gigawatts of photovoltaic (PV) integration.

Achieving the ambitious goals set forth by the U.S. Department of Energy's SunShot Initiative will require an increase in installed PV by hundreds of gigawatts during the next several decades. Because existing grid operations are predicated on the presence of significant rotational inertia from large collections of synchronous machines, and because PV inverters are power electronic devices with no inherent inertia, it follows that the SunShot targets for PV adoption present a direct challenge to existing practices. The aim of the proposed project is to develop a suite of inverter controllers that ensure the long-term viability of the electrical infrastructure and address obstacles precipitated by increased inverter adoption and the accompanying reduction in system-wide inertia. To achieve these goals, we advocate for the development of what we call GFM inverter controllers—that is, the inverter will act as a controllable voltage source that dynamically adjusts its output to ensure system-level stability, synchronization, and voltage regulation (see Figure 1(b)). This approach represents a departure from existing GFL PV inverter controls that are controlled to inject a current in phase with their terminal voltage such that maximum available PV power is delivered at all times. These conventional controllers, as illustrated in Figure 1(a), are built on the assumption that transmission-level generators maintain system integrity.

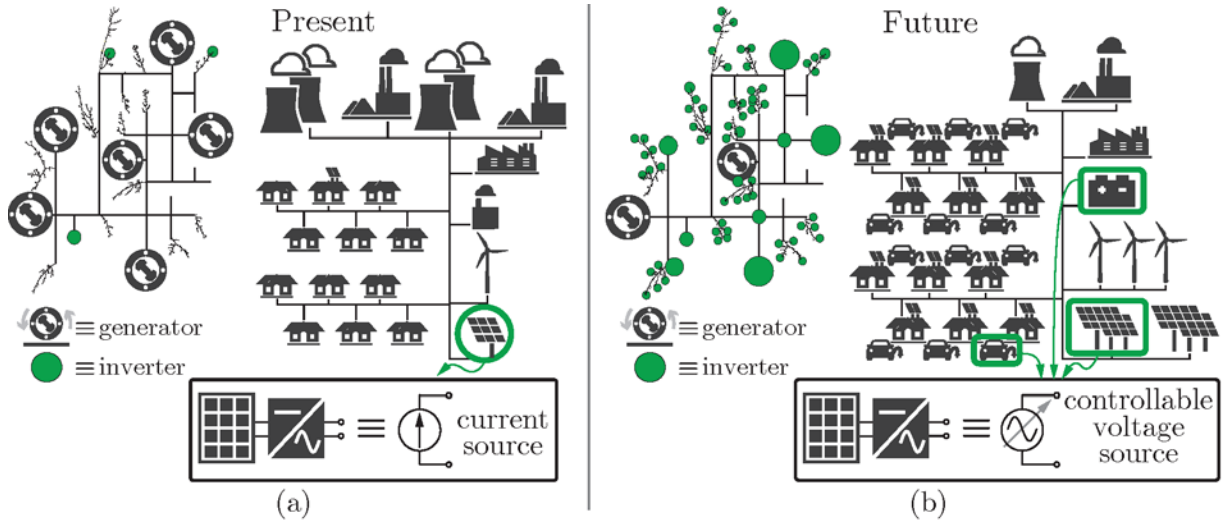

Figure 1. The existing power system (a) is dominated by synchronous generators having large rotational inertia with a relatively small amount of inverter-interfaced PV. Existing PV inverters are controlled to act as GFL current sources. The proposed inverter controller enables the future architecture in (b), which is dominated by PV- and storage- interfaced inverters at the distribution and transmission scales. Each GFM inverter acts as a controllable voltage source that rapidly stabilizes system dynamics.

We advocate for a strategy for the modeling, design, and analysis of GFM inverter controllers based on the emergence of synchronization in networks of coupled oscillators. The essence of the proposed method is to digitally control each power electronic inverter to emulate the

dynamics of a nonlinear oscillator (See Figure 2). With this strategy in place, it can be shown that the intrinsic electrical coupling between inverters promotes system-wide synchronization—a stable and self-synchronizing power system emerges by design. A key component of our approach is to ensure backward compatibility of the proposed method by incorporating drop-in replacement interoperability with existing approaches. This approach facilitates a gradual evolution of the electric grid to a network driven by inverters and eases industry adoption.

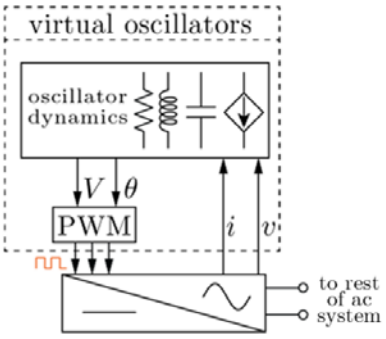

Figure 2. Diagram of implementation of an oscillator-based controller on a PV inverter. The energy source is connected to the grid through a VOC inverter.

A comprehensive commercialization strategy has been formulated that entails a joint effort between the National Renewable Energy Laboratory (NREL) and SunPower in translating the finalized GFM controllers into practical implementations on commercial inverter hardware. Today, SunPower is one of the largest manufacturers of PV modules and is aggressively pursuing the development of next-generation inverters. In the last phase of the project, the completed controls and hardware were validated in complex hardware-in-the-loop (HIL) experiments that capture the dynamic interactions between the multiple GFM inverters in a low-inertia setting. An extensive dissemination plan ensures that results will be conveyed to the industrial research-and-development community, academia, practicing power industry professionals, and students.

Following is an overview of the project tasks in the three budget periods:

- Budget Period 1 contained three tasks:
    - In Task 1.1, we focused on developing an analytical modeling framework for systems with traditional GFL controllers. We observed that the system could become unstable as we increased inverter-based resources with GFL inverters, establishing a need for novel GFM methods.
    - In Task 1.2, we focused on developing a particular class of GFM inverter controllers, the VOC, that actively enforces stability bounds.
    - In Task 1.3, we promoted industry acceptance by ensuring compatibility of the proposed GFM controllers with essential features in use today.
- Subsequently, in Budget Period 2, we enabled major advances in understanding the system-level properties of GFM controllers and their ability to regulate terminal voltage and preserve system stability. The hardware and experimental work were pivotal in

developing the envisioned implementations and validating the analytical framework. Specifically, we continued with two tasks:

  - In Task 2.1, we used the analytical framework and test scenarios developed in Budget Period 1 to characterize the tipping point of systems with conventional GFL controllers and analyzed the transient stability of systems with the proposed GFM controls.
  - In Task 2.2, we focused on the experimental validation of the analytical models and the controller board hardware development.

- Last, in Budget Period 3, we completed the following tasks:
  - In Task 3.1, we developed a comprehensive modeling framework and accompanying case studies for the stability assessment of low-inertia grids.
  - In Task 3.2, we evaluated the performance of the proposed GFM controllers in a set of experiments and simulations that reflect a spectrum of operational conditions. We also created a research road map for GFM inverter research that outlines the state of the art in this area and future research directions.

These activities were designed to reach the overarching project objectives through a tiered project plan that yields pertinent models, prototypes, and realistic experiments and culminates in the launch of a commercial product.

3 Project Results and Discussions

During the project, our team pursued developments in three key areas as encapsulated in the project tasks. The tasks were structured such that we first modeled and investigated the limitations of conventional GFL inverter controllers in low-inertia settings. The second task focused on designing, analyzing, and validating next-generation GFM inverter controllers and how they compare to existing inverter control methods. Last, the team created a research road map for GFM inverter that outlines the state of the art in this area and future research directions.

In this section, we provide a summary of the project outcome of each subtask in the project evaluation criteria tables. More detailed technical descriptions are provided in the sections following the tables.

Table 1. Task 1.1. Develop Flexible Models and Test Scenarios for Stability Analysis of Systems with GFL Inverters

	Metric Definition (From Measurement)	Success Value	Measured Value	Assess-ment Tool (Quality Assurance)	Goal Met (Y/N)	Supporting Data (pg. #)
Project Evaluation Criteria 1.1a	Results from analytical system model match those from detailed network model	Demonstrate that the analytically derived time-domain model is stable (unstable) when the detailed accurate model is stable (unstable) under the developed test scenarios	Zero steady-state error between analytical and detailed inverter models	Numerical simulation via MATLAB/ Simulink simulation of dynamic network model using SimPower-Systems	Yes	Pages 12–16
Project Evaluation Criteria 1.1b	Publication of analytical modeling framework in a peer-reviewed publication	Submitted manuscript of paper	Papers published in COMPEL and NAPS	Peer-review publication	Yes	Conference papers published

Table 2. Task 1.2. Develop a Constraint-Enforcing Storage Controller That Is Capable of Enforcing Power-Flow Constraints in a Network

	Metric Definition (From Measure-ment)	Success Value	Measured Value	Assessment Tool (Quality Assurance)	Goal Met (Y/N)	Supporting Data (pg. #)
Project Evaluation Criteria 1.2a	Completed design of CED controller	Successful integration of CED with storage energy management to (1) enforce power flow constraints adjacent to CED inverter (no more than ¼ AC cycle overshoot), and (2) enforce physical limits of the energy storage device	(1) Successfully enforced line limits with zero overshoot, and (2) physical limitations of storage device were successfully enforced.	Dynamic software simulation of CED inverter	Yes	Pages 16–17
Project Evaluation Criteria 1.2b	Validation of CED functionality by benchtop-scale experiment	Validate ability of CED to (1) enforce power flow constraints adjacent to CED inverter (no more than ¼ AC cycle overshoot), and (2) enforce physical limits of energy storage device	Based on DOE feedback at Phase 1 continuation review, this effort has been canceled.	Measure-ments on hardware im-plementation of CED	Canceled[1]	N/A

[1] Some key limitations of this approach were discovered. Accordingly, because of active project management from the principal investigator and feedback from DOE, the experimental efforts on this task were canceled, and efforts were redirected to other tasks.

Table 3. Task 1.3. Develop GFM Inverter Controllers That Serve as Drop-in Replacements for Existing Controllers

	Metric Definition (From Measurement)	Success Value	Measured Value	Assessment Tool (Quality Assurance)	Goal Met (Y/N)	Supporting Data (pg. #)
Project Evaluation Criteria 1.3a	MPPT and curtailment functionality of GFM controller for PV	GFM controller should track maximum power point and curtailment commands with <5% error and <1-s settling time.	Maximum power point is tracked with zero error, and curtailment command is followed with negligible error.	(1) Simulation, and (2) electrical measurements of developed PV inverter prototype	Yes	Pages 24–25
Project Evaluation Criteria 1.3b	Real/reactive power ("fixed P/Q") dispatchability and droop functionality of GFM storage inverter	GFM P/Q controller should track real and reactive power commands with <5% error and <1-s settling time and track a frequency/W curve with an error of <0.1 Hz and a settling time of <1 s.	P/Q commands followed with zero error and settling time <1 s. Desired frequency/W curves followed with error <0.1 Hz and settling time <1 s.	(1) Simulation, and (2) electrical measurements of developed storage inverter prototype	Yes	Pages 18–24
Project Evaluation Criteria 1.3c	GFM capabilities of a cluster of inverters with the proposed controllers	Cluster of interconnected inverters should form a stable AC system in the absence of communication or a reference signal	All objectives met in simulation and hardware.	1) Simulation, and (2) electrical measurements of developed inverter prototype	Yes	Pages 21–22, 31–35

Table 4. Task 2.1. Develop Models of Low-Inertia Grids with Traditional GFL Controllers and Characterize Their Stability As a Function of Mechanical Inertia and Renewable Penetration

	Metric Definition (From Measurement)	Success Value	Measured Value	Assessment Tool (Quality Assurance)	Goal Met (Y/N)	Supporting Data (pg. #)
Project Evaluation Criteria 2.1a	Quantitative relationship between renewable energy penetration (0%–100% instantaneous levels) and system inertia	Methodology established that translates renewable energy penetration to the ratio of inverter and synchronous machine capacity ratings for the system	Developed methodology to translate renewable energy penetration to inverter-machine capacity rating ratio	Analytical or algorithmic framework	Yes	Pages 31–35
Project Evaluation Criteria 2.1b	Scalable software models to assess multi-inverter, multi-synchronous-machine systems with varying levels of inertia	At least one meshed and one radial IEEE test circuit are executed in software with varying levels of inertia	Software models developed	Software simulation of model	Yes	Pages 35–39
Project Evaluation Criteria 2.1c	Existence of tipping point	Numerical simulations and supporting analysis demonstrate the hypothesized "tipping point" exists	(1) Existence of tipping point established in simple single-inverter, single-machine model, and (2) existence of tipping point in representative multi-inverter, multi-machine systems	Software simulation and supporting analysis	(1) Yes (2) Yes	Pages 35–39
Project Evaluation Criteria 2.1d	Comparison of stability analysis using analytical model vs. detailed software dynamic model	PV penetration at which stability is lost as determined from software simulation is within ±20% of the analytical result.	(1) Confirmed in simulations for single-inverter, single-machine system, and (2) confirmed in representative multi-inverter, multi-machine systems	MATLAB/ Simulink simulation of dynamic network model	(1) Yes (2) Yes	Pages 35–39
Project Evaluation Criteria 2.1e	Report on tipping point results	Finalized report on stability analysis results	Delivered report/publication with the relevant findings	Technical report	Yes	Conference paper published

Table 5. Task 2.2. Develop, Validate, and Compare the Performance of GFM Controllers in Systems with Variable Inertia

	Metric Definition (From Measurement)	Success Value	Measured Value	Assessment Tool (Quality Assurance)	Goal Met (Y/N)	Support-ing Data (pg. #)
Project Evaluation Criteria 2.2a	Performance comparison of VOC with competing GFM control methods	Response time, settling time, and magnitude of transients are characterized/ compared for multi-inverter experiments with oscillator-based and droop control.	Dynamic characteris-tics of droop- and oscillator-based inverters compared	Electrical measurements on test bed	Yes	Pages 25–27
Project Evaluation Criteria 2.2b	Functionality of commercial SunPower inverter with VOC	Firmware of SunPower inverter has been modified such that the inverter executes VOC and functions as a self-organizing microgrid with no stiff grid	Measure-ments of more than one inverter showing ability to form a zero-inertia grid	Electrical measurements on SunPower inverter	Yes	Page 41–50
Project Evaluation Criteria 2.2c	Comparison of experimental results with numerical simulations	Frequency response of inverter test bed with inertia emulation matches software model of machine/inverter system within 20% of error during a load step	Measure-ments of emulated machine with variable inertia closely match simulation	Electrical measurements on test bed	Yes	Page 29–30

Table 6. Task 3.1. Develop a Comprehensive Modeling Framework and Accompanying Case Studies for Stability Assessment of Low-Inertia Grids

	Metric Definition (From Measurement)	Success Value	Measured Value	Assessment Tool (Quality Assurance)	Goal Met (Y/N)	Support-ing Data (pg. #)
Project Evaluation Criteria 2.1d	An aggregation scheme to obtain feeder-level equivalents	Set of simulation results showing that the time-domain response of a feeder system is accurately captured with the proposed aggregated equivalent model	Developed a reduced-order model to represent a feeder	MATLAB/ Simulink simulation of model	Yes	Pages 31–35
Project Evaluation Criteria 3.1a	Stability analysis of a large-scale, multi-inverter, multi-synchronous-machine system model that resembles a transmission	Existence of analytical framework that characterizes system stability	Stability analysis performed on IEEE 39-bus system	Mathematical framework	Yes	Pages 35–39
Project Evaluation Criteria 3.1b	Comparison of analytically derived results and detailed software dynamic models	Confirmation of tipping point analysis by comparison of detailed time-domain model and analytical results	Confirmed the tipping point analysis is consistent with time-domain model	MATLAB/ Simulink simulation of dynamic network model	Yes	Pages 35–39
Project Evaluation Criteria 3.1c	Report on finalized tipping point analysis framework and results	Finalized report on stability analysis results	Confer-ence paper published	Technical report	Yes	Conference paper published

Table 7. Task 3.2. Validate the Performance of GFM Controllers in Complex Systems, Create Road Map for System-Wide Adoption, and Disseminate Control Code in Publicly Available Format

	Metric Definition (From Measurement)	Success Value	Measured Value	Assess-ment Tool (Quality Assurance)	Goal Met (Y/N)	Supporting Data (pg. #)
Project Evaluation Criteria 3.2a	Comparison of transient stability characteristics for systems with either GFM or existing GFL controls	Models and experiments demonstrate that systems with GFM controllers can maintain stability in zero-inertia settings, whereas conventional GFL controllers cannot.	Demon-strated through simulation and experiments	Simulation results and experimental measure-ments	Yes	Pages 41–50
Project Evaluation Criteria 3.2b	Simulation of a very large-scale, zero-inertia system with proposed GFM controllers	Software model that is representative of a transmission system with more than 100 nodes where each synchronous generator has been replaced with a GFM inverter	Positive-sequence load flow simulation performed on IEEE 39-bus system and the MicroWECC system	Software model	Yes	Pages 50–52
Project Evaluation Criteria 3.2c	Validation of a multi-inverter, zero-inertia system with a mix of conventional PV inverters and GFM inverters	Multi-inverter experimental setup consisting of a mix of next-generation GFM controllers operating alongside conventional PV GFL inverters with realistic network elements such as a capacitor bank and network impedances	Validated with SunPower 20-microinverter test bed	Experimen-tal measureme nts	Yes	Pages 41–50
Project Evaluation Criteria 3.2d	Finalized plans for workshop on GFM controls and low-inertia grids	Workshop will feature speakers and attendees from DOE labs, industry, and academia with leading expertise in low-inertia grids.	Per DOE request, the workshop was not hosted within the project.	Attendance by DOE staff	Canceled[2]	N/A
Project Evaluation Criteria 3.2e	Report outlining the properties of the finalized controllers and road map with future adoption scenarios	Report outlining the advantages of the finalized controllers as well as a road map of remaining challenges for realizing large-scale grid transformations and envisioned pathways forward	Roadmap published	Technical report	Yes	Roadma p published

[2] After discussion with DOE, it was decided that the workshop should be held outside of this project because of logistical considerations. Accordingly, the project team hosted the Workshop on Grid-Forming Inverters for Low-Inertia Power Systems outside of this project at the University of Washington in 2019.

Next, we present the technical details related to the project outcomes. For better demonstration, the discussion is organized by topic. Each topic might be related to multiple tasks.

3.1 Develop Flexible Models for Stability Analysis of Systems with Grid-Following Inverters (Associated with Tasks 1.1 and 2.1)

In this section, we discuss the inverter and machine models developed in the project. To facilitate the stability analysis, the team developed both detailed and approximate "reduced-order" models for GFL inverters. We demonstrated that the detailed GFL inverter model and the analytically derived approximate model closely resemble each other.

A conventional GFL inverter and its accompanying controller containing a PLL is shown in Figure 3. In this system, we begin by assuming that the grid voltage, v_b, is regulated by an external entity (e.g., a machine). For simplicity, we first assume that v_b is fixed by a stiff AC grid. The output LCL filter circuit that interfaces the inverter to the grid is used to suppress noise and harmonics generated by the switching power electronics. The remaining control blocks are digitally implemented within the inverter digital controller. In general, the structure shown in Figure 3 represents common practice and is used ubiquitously in industry.

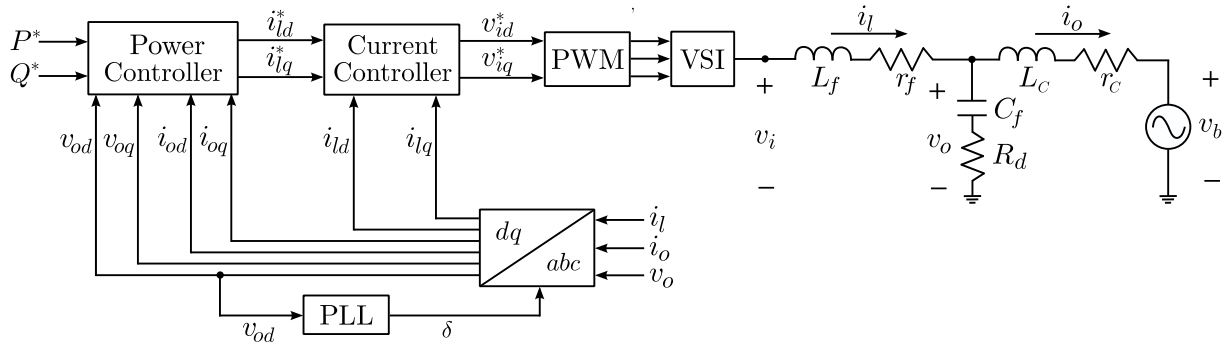

Figure 3. Block diagram of three-phase inverter. The blocks labeled "Power Controller," "Current Controller," "dq/abc," and "PLL" are controller blocks (software); whereas the blocks labeled "PWM" and "VSI" are physical blocks (hardware). Because we assume that the inverter is ideal, we assume that vi = vi*.

3.1.1 Derivation of Detailed Inverter Model

We begin by deriving the dynamics of the detailed model as illustrated in Figure 3. Here, we present the model concisely; more details are reported in Lin et. al. (2017). Signals that are subscripted with *d* or *q* are signals that have undergone a coordinate transformation; otherwise they are AC. The system has 15 states: i_{ld}, i_{lq}, i_{od}, i_{oq}, v_{od}, v_{oq}, Υ_d, Υ_q, P_{avg}, Q_{avg}, ϕ_P, ϕ_Q, $v_{od,f}$, ϕ_{PLL}, and δ, where the first 6 states are for the LCL filter, the next 2 states are for the current controller, the next 4 states are for the power controller, and the last 3 states are for the PLL. From a modeling standpoint, the inputs are the real and reactive power commands, denoted by P* and Q*, respectively, and the grid voltage, v_b. The frequency of the grid is denoted by ω_g where we begin by assuming $\omega_g = 2\pi 60$ rad/s. The model is developed in the dq frame, where Park's transformation is used to transform balanced, three-phase sinusoidal signals to equivalent DC signals.

The components shown in Figure 3 that are modeled include the PLL, LCL filter, current controller, and power controller. Because of limited space, we do not list the dynamic equations for each component. Instead, we use a compact notation. Let x denote the vector of the states of the system, and let u denote the model inputs. In this case:

$$x := [i_{ld},\, i_{lq},\, i_{od},\, i_{oq},\, v_{od},\, v_{oq}, \gamma_d,\, \gamma_q,\, P_{\text{avg}},\, Q_{\text{avg}},\, \phi_P,\, \phi_Q,\, v_{od,f},\, \phi_{\text{PLL}},\, \delta]^{\text{T}},$$
$$u := [P^*,\, Q^*,\, v_{bd},\, v_{bq}]^{\text{T}}.$$

The system dynamics can be written in compact form:

$$\dot{x} = Ax + Bu + g(x),$$

3.1.2 Derivation of Analytical Approximate Inverter Model

Having derived the detailed model, we now proceed to the derivation of the reduced-order analytical model. The reduced-order model is derived using the singular perturbation method. The dynamics of the full-order model are normalized as follows:

$$\left[\frac{L_f}{r_f}\dot{i}_{ld} \quad \frac{L_f}{r_f}\dot{i}_{lq} \quad \frac{L_c}{r_c}\dot{i}_{od} \quad \frac{L_c}{r_c}\dot{i}_{oq} \quad \frac{C_f}{r_d}\dot{v}_{od} \quad \frac{C_f}{r_d}\dot{v}_{oq} \quad \frac{\text{kp}_{id}}{\text{ki}_{id}}\dot{\gamma}_d \quad \frac{\text{kp}_{iq}}{\text{ki}_{iq}}\dot{\gamma}_q \quad \frac{1}{\omega_c}\dot{P}_{\text{avg}} \quad \frac{1}{\omega_c}\dot{Q}_{\text{avg}}\right.$$
$$\left.\frac{\text{kp}_P}{\text{ki}_P}\dot{\phi}_P \quad \frac{\text{kp}_Q}{\text{ki}_Q}\dot{\phi}_Q \quad \frac{1}{\omega_{c,\text{PLL}}}\dot{v}_{od,f} \quad \dot{\phi}_{\text{PLL}} \quad \dot{\delta}\right]^T.$$

where k are the controller gains. Let y denote the vector of slow states, and let z denote the vector of fast states. Using the parameters in Table I and Table II in Rasheduzzaman, Mueller, and Kimball (2015), we select the slow states as $y = [P_{avg}, Q_{avg}, \phi_P, \phi_Q, \phi_{PLL}, \delta]^T$ and the fast states as $z = [i_{ld}, i_{lq}, i_{od}, i_{oq}, v_{od}, v_{oq}, \Upsilon_d, \Upsilon_q, v_{od,f}]^T$. The dynamics of the slow and fast subsystems can be written as:

$$\dot{y} = f(y, z, u, \varepsilon)$$
$$\varepsilon\dot{z}(t) = g(y, z, u, t, \varepsilon),$$

where ε is the parameters of the fast states. To reduce the number of states, we set ε = 0, so that the fast dynamics are described by algebraic equations; thus, we have differential and algebraic equations as follows:

$$\dot{y} = f(y, z, u, 0)$$
$$0 = g(y, z, u, t, 0).$$

This completes the derivation of the reduced-order model. Note that whereas the original model had 15 states, the reduced-order model has only 6 state variables (as indicated by the number of variables in the vector y). Accordingly, the model complexity is reduced by more than a factor of two. Next, we compare the dynamics of the reduced-order model with the states in y and the original detailed model. Also, note that the analysis shows that the PLL variables (ϕ_{PLL}, δ) account for the slowest state variables in the controller.

3.1.3 Comparison of the Detailed and Approximate Analytical Models

Next, we provide plots for both the fast and slow variables in the approximate reduced-order model and compare them to the original states in the detailed model. In the following simulation, we use the parameters in Rasheduzzaman, Mueller, and Kimball (2015) and consider the scenario where there is a step change in the real power command from 0 W to 500 W. The reactive power command is fixed at zero. This scenario could represent a sudden increase in PV irradiance. The filtered real and reactive power are plotted in Figure 4 and Figure 5, where it is apparent that the reduced-order model provides a relatively accurate approximation of the detailed inverter model. Although the transient behavior is different in the two models because of reducing the fast states, the steady-state error is zero.

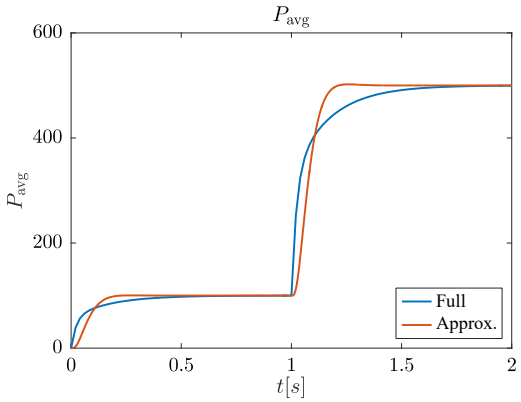

Figure 4. Comparison of simulated states in the reduced-order model to the original full-order detailed model (P)

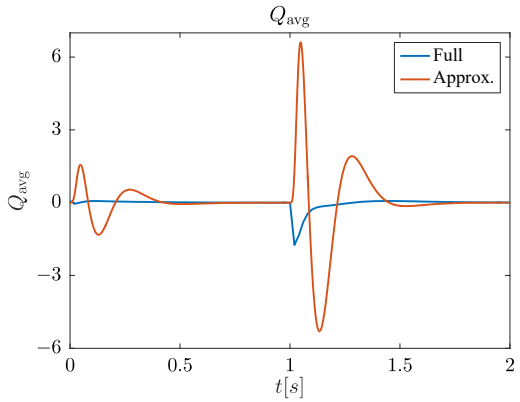

Figure 5. Comparison of simulated states in the reduced-order model to the original full-order detailed model (Q)

3.1.4 Synchronous Machine Model

We adopted a standard machine model (Kundur, Balu, and Lauby 1994). The model includes a prototypical machine, exciter, and prime mover model for a steam-driven coal power plant. The model contains two main loops: the frequency dynamics and the voltage dynamics. In the frequency loop, the derivative of the frequency is determined by the well-known swing equation. The electric power acting on the rotor is calculated from the voltage loop variables. The mechanical power is provided by the steam turbine, whose dynamics can be approximated by a second-order system. The droop control law is achieved by the governor and the droop slope.

In the voltage loop, the voltage controller maintains the terminal voltage at its reference by controlling the exciter, which produces the field voltage. The voltage controller is modeled as a lead-lag compensator, and the exciter is modeled as a first-order system. With some simplification assumptions, the electromagnetic dynamics can be approximated by a first-order system, with the field flux linkage as the state. The terminal voltage can be expressed as an algebraic function of the system states and inputs.

Here, we describe the model concisely; more details are reported in Lin et. al. (2017). The inputs of the synchronous machine model are:

$$u_m = \left[v^*, P_{agc}, i_{m,dq}\right]^{\mathrm{T}},$$

where v^* is the terminal voltage set point, P_{agc} is the automatic generation control power reference, and $i_{m,dq}$ are the terminal currents. The states of the machine model are:

$$x_i = [\theta_g, \omega, P_g, P_{gt}, P_m, v_c, v_{fd}, \lambda_{fd}]^{\mathrm{T}} ,$$

where θ_g is the rotor angle, ω is the frequency, P_g is the state for the governor, P_{gt} is the state for the steam turbine, P_m is the mechanical power on the rotor, v_c is the state for voltage controller, v_{fd} is the field voltage, and λ_{fd} is the field flux linkage.

In compact form, we can write the machine model as:

$$\dot{x}_m = f(x_m, u_m) .$$

3.2 Develop a Constraint-Enforcing Storage Controller That Is Capable of Enforcing Power Flow Constraints in a Network (Associated with Task 1.2)

Future distribution systems with high penetrations of distributed energy resources will be dominated by power electronics, and as such they will require new methods of control to ensure network stability and physical constraints. A novel control architecture for such systems based on coupled-oscillator methods is presented here; however, such a method will require the active enforcement of a set of power flow constraints on lines. To fulfill this role, we developed a novel controller type for inverter-interfaced battery energy storage systems, which we call the constraint-enforcing droop (CED). This section presents the proposed controller design, along with the simulation validation of its ability to enforce the specified line power flow constraints while protecting and managing the state of charge of the battery. Results show that the project metrics are largely satisfied by the proposed controller.

The key capabilities of the constraint-enforcing inverter are as follows:

1. Enforce a specified line power flow constraint on an adjacent line. This constraint is of the form $|P_{line}(t)| \leq P_{line,max}$, where $P_{line}(t)$ is the real-time measured power flow on the specified line, and $P_{line,max}$ is the specified maximum value of the line power flow on that line.
2. When the specified line power flow constraint is not violated, the controller should behave identically to a baseline VOC.
3. The controller manages the state of charge of the energy storage device at the input to ensure that the device in not fully discharged or overcharged.

These capabilities of the CED inverter are illustrated in Figure 6. Collectively, these plots demonstrate that all the criteria for Task 1.2 have been satisfied except for the overshoot time target.

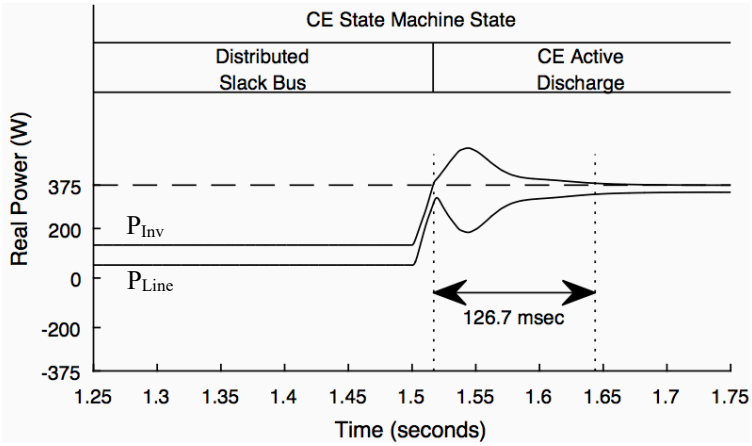

Figure 6. Constraint enforcing controller dynamic response test results. The top plot shows the state of the management machine. The lower plot shows the P Line **(solid black), which remains below the line limit P**Line,Max **(dashed black), and the inverter output power, P**Inv **(solid gray).**

3.3 Develop Grid-Forming Inverter Controllers That Serve as Drop-In Replacements for Existing Controllers (Associated with Tasks 1.3 and 2.2)

This topic encapsulates the development work for the GFM controllers. To ensure drop-in replacement compatibility, the team developed a baseline GFM VOC, a PQ tracking VOC, and, last, a version of the controller that is compatible with PV.

These three GFM controllers are all based on the VOC approach developed in prior work (Johnson et. al. 2015). VOC is a time-domain control approach in which the inverter is programmed (through its digital controller) to emulate the dynamics of a nonlinear electrical oscillator, as shown in Figure 7. Prior work showed that a network of multiple inverters implementing this control method will naturally synchronize to an AC limit cycle with voltage and frequency within specified limits. Because all three controller types developed in this project are based on VOC, they all inherit its natural synchronization and voltage/frequency management properties, and therefore they are capable of GFM in ways that the existing controller types that they replace are not.

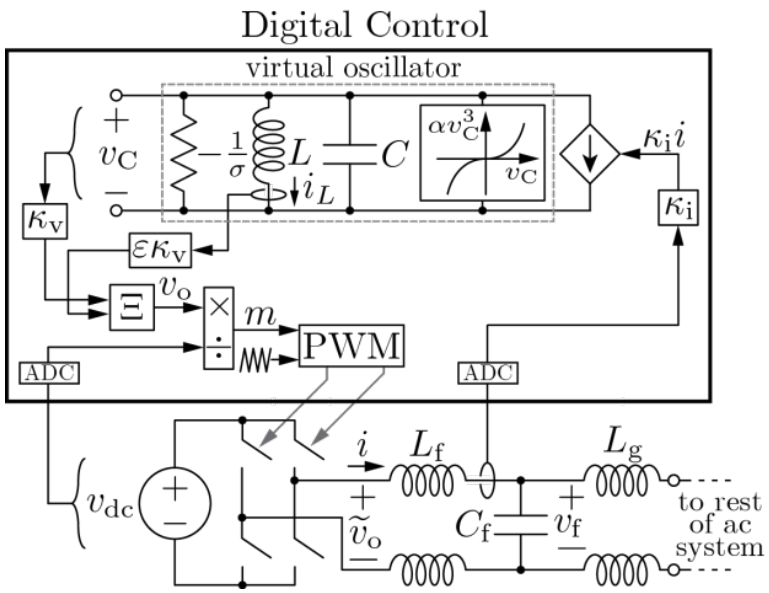

Figure 7. Block diagram of the VOC approach. In this approach, the digital controller implements the dynamic equations describing a nonlinear Van der Pol-type oscillator. The inverter voltage is then controlled to track a scaled combination of the virtual capacitor voltage and inductor current. Finally, the loop is closed through feedback of the inverter output current.

3.3.1 Baseline Grid-Forming Virtual Oscillator Controller

The baseline GFM VOC controller must maintain system voltage and frequency within specified limits while sharing power with the other inverters and synchronous generators in the network. In existing microgrid systems, this effect is often achieved by the so-called "droop" control method, which is inspired by the governor action in traditional synchronous generator systems. In droop control, the real and reactive power output of the inverter are explicitly calculated from real-time measurements, and the inverter voltage and frequency set points are adjusted based on a set of quasi-static equations. In theory, this method results in the synchronization of the droop inverters to each other in frequency and sharing the network slack real and reactive power between the inverters proportional to their droop slopes (thus, we use the term "distributed slack bus").

In practice, however, the time constant of the droop controller is limited by the need to explicitly calculate real and reactive power, which is not well defined from subcycle measurements. As a result, droop-controlled inverters are often unable to respond quickly enough to ensure network stability and security in the face of fast distribution network dynamics, such as large load shifts or loss of line/generation. In particular, it is not possible to meet the 1-second settling time requirement in Project Evaluation Criteria 1.3a-b using droop control; therefore, another control method is needed that achieves a similar distributed slack bus effect but that can respond to real-time measurements on a subcycle basis.

Prior work (Johnson et. al. 2015) showed that a VOC inverter exhibits a natural "droop" relationship at its limit cycle in which voltage decreases with increasing real power (we call this effect P-V droop), and frequency decreases with increasing reactive power (Q-ω droop). Because of its resemblance (at a slow timescale) to the traditional quasi-static droop laws for resistive networks, we call this type of controller resistive VOC; however, the project targets are based on

the so-called "inductive" droop laws, in which frequency decreases with increased real power (P-ω droop) and voltage decreases with increased reactive power (V-Q droop).

Because it is a time-domain controller that responds to real-time measurements, VOC can respond to changes in network dynamics much more quickly than traditional droop controllers; therefore, VOC is a strong candidate to fulfill the distributed slack bus function traditionally assigned to droop inverters (for either resistive or inductive networks) while meeting the project timing requirements. To enable the VOC to fully achieve this function, however, it must be made possible to adjust the limit-cycle droop relationships exhibited by VOC so they can be made to resemble either the "resistive" (P-V, Q- ω) or "inductive" (P- ω, Q-V) droop laws. This can be achieved by adjusting the parameters of the scaled combination of virtual capacitor voltage and inductor current used to generate the inverter voltage command.

We have therefore introduced two kinds of baseline GFM VOCs for distributed slack bus functionality: one based on the original resistive VOC (which exhibits the P-V, Q- ω droop characteristic) and the other based on the modified inductive VOC (which exhibits the P- ω, Q-V characteristic). Next, we show results from detailed power electronics simulations that demonstrate the performance of both controllers and compare their performance to the project task targets. Then we consider a network of resistive VOC-type inverters and show their ability to self-form an islanded grid, respond to load steps, and add/remove inverters to/from an energized network while sharing real and reactive power and regulating voltage and frequency to within specified limits.

3.3.1.1 Single-Inverter Performance

Consider a simple system consisting of a single GFM inverter coupled to a constant-impedance load. We will use this system as the basis for demonstrating the performance of the baseline GFM VOC (in both its resistive and inductive forms) that responds to changes in the real and reactive power at its terminals.

As part of the SunLamp project, NREL and the University of Minnesota developed design procedures for GFM distributed slack bus controllers based on both resistive and inductive VOCs. These design procedures allow standard AC performance specification (e.g., voltage regulation limits, frequency error limits, power ratings) to be translated into a controller design and set of VOC parameters that ensure that the specifications are met. In addition, this procedure allows the controller to be designed so that it implements a specified set of droop curves (the P-V, Q- ω for resistive VOC or P- ω, Q-V for inductive VOC).

We followed the design procedures in Johnson et al. (2015) and Sinha et al. (2015a) to design two baseline VOCs (based on resistive VOC and inductive VOC respectively). We then simulated the resulting controllers in the system consisting of a single inverter and load. Next, we assessed their droop performance by adjusting the impedance of the load, allowing the oscillator to settle to its limit cycle, and then we recorded the resulting magnitude and frequency of the AC voltage at the terminals of the inverter.

Figures 8 and 9 shows the resulting droop curves for the resistive and inductive GFM distributed slack bus controllers, respectively, where the x's are the steady-state voltage and frequency results from detailed simulation, and the dashed lines are the target droop curves shown in Table

8. Notice that the resistive controller correctly tracks the target P-V and Q-f droop curves with minor errors because of the nonlinearity of the VOC. Similarly, the inductive controller correctly tracks the target P-f and Q-V droop curves with minor offsets. These results verified that both GFM distributed slack bus controllers were able to track the specified droop curves with less than 1% error (relative to nominal voltage/frequency), thus satisfying Project Evaluation Criteria 1.3b.

Table 8. System Parameters

Parameters	Description	Value		Unit
		Resistive VOC	Inductive VOC	
Vmax	Max voltage	126	126	Vrms
Vmin	Min voltage	114	114	Vrms
foc	Open-circuit frequency	60	60	Hz
fmin	Min frequency	60.5	60.5	Hz
fmax	Max frequency	59.5	59.5	Hz
Rqf	Q-f droop slope	-0.00067	N/A	Hz/Var
Rpv	P-V droop slope	-0.008	N/A	Vrms/W
Rpf	P-f droop slope	N/A	-0.00067	Hz/W
Rqv	Q-V droop slope	N/A	-0.008	Vrms/Var

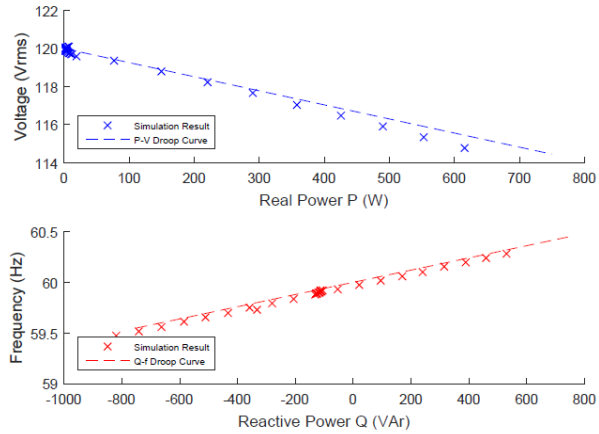

Figure 8. Droop performance of resistive GFM distributed slack bus controller from simulation

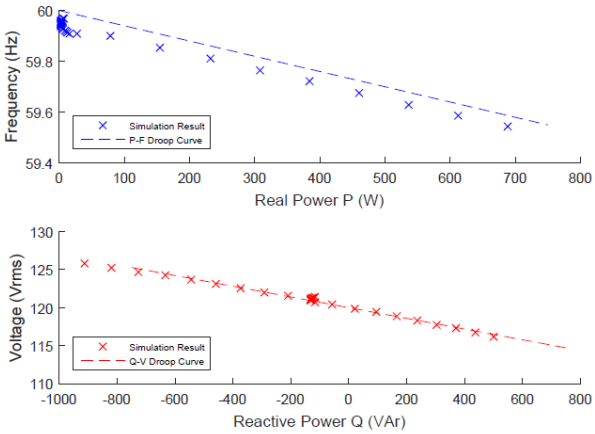

Figure 9. Droop performance of inductive GFM distributed slack bus controller from simulation

3.3.1.2 Multi-Inverter Synchronization and Performance

Although these results show the ability of the GFM distributed slack bus controller to track specified droop slope curves and therefore to meet Project Evaluation Criteria 1.3b, the key capability of the new controller is its ability to self-form an islanded power system with other similar controllers (Project Evaluation Criteria 1.3c). In the following simulation, we show this

capability in a simple islanded system consisting of five parallel inverters connected to a single load bus. In this simulation, we demonstrate the following functions of the baseline VOCs:

1. Black-start of a loaded network by a single inverter
2. Synchronization and connection of subsequent inverters to the (already energized) network
3. Response of the multi-inverter network to both real and reactive load steps
4. Removal of an active inverter from the energized network and subsequent response of the remaining inverters

In each condition, the GFM controllers must maintain system voltage and frequency within the limits set in Table 8 while equally sharing the real and reactive power of the load (that is, acting as a distributed slack bus). In addition, the system as a whole should exhibit the voltage and frequency droop characteristics appropriate to the selected droop type (resistive or inductive).

Figure 10 10 and Figure 11 show the results of the simulation in which all inverters implement the resistive or inductive GFM controllers, respectively (inverter traces are colored, load traces are black). In both simulations at t = 0 second, Inverter 1 is switched on. After a brief controller startup period, Inverter 1 performs a black-start of the network with a load equal to approximately 500 W (approximately two-thirds of its rated power), reaching a voltage and frequency based on its assigned droop curves (P-V and Q-f for the resistive controller, P-f and Q-V for the inductive controller). Then, at t = 0.5, 1.0, 1.5, and 2.0 seconds, the subsequent inverters 2–5 are added to the network. In each case, the added inverter synchronizes to the existing voltage on the network, closes to it, and then all the inverters respond to equalize their sourced real and reactive power values, converging to a new voltage and frequency steady-state again based on the assigned droop curves. At t = 2.5 and 3.0 seconds, additional real and reactive load are stepped onto the load bus, resulting in a convergence of the inverters to a new steady state in which real and reactive power are equally shared, and a new voltage and frequency equilibrium is reached. Finally, at t = 3 seconds, Inverter 1 is shut off, resulting in its power rapidly reducing to zero and the remaining inverters sharing the total system load.

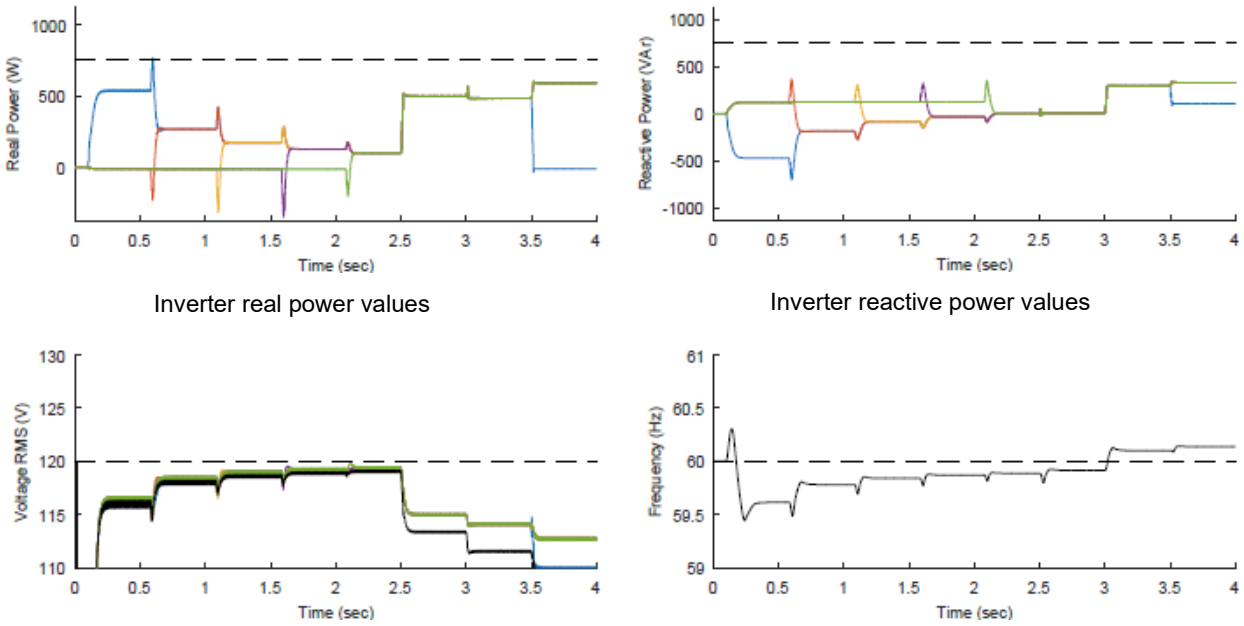

Figure 10. Multi-inverter islanded simulation for resistive VOC

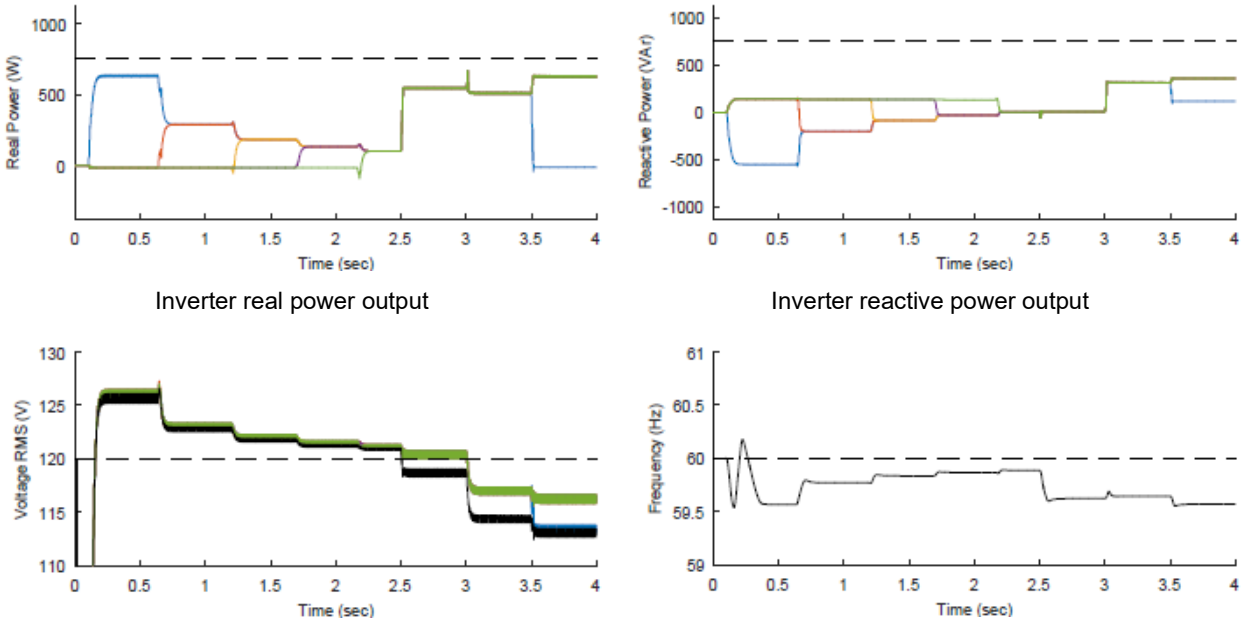

Figure 11. Multi-inverter islanded simulation for inductive VOC

These multi-inverter simulations show the ability of both GFM distributed slack bus controllers to self-form an islanded network, synchronize to each other and share power, respond to load changes, and add and remove devices while energized, all while maintaining system voltage and frequency within the specified limits. This demonstrates that both GFM controllers (resistive and inductive) meet the requirements in Project Evaluation Criteria 1.3c.

3.3.2 Grid-Forming Real/Reactive Power (P/Q) Tracking Controller

The second major type of GFM inverter controller developed under this project is the GFM real/reactive power (P/Q) tracking controller. When the grid voltage and frequency is within the prescribed limits, this controller is designed at steady state to inject commanded real and reactive power into the network. Although this effect can be achieved at steady state using traditional GFL current controller types, the novel function of GFM P/Q tracking controller is twofold:

1. The GFM P/Q tracking controller has transient behavior that assists in grid synchronization and supports the system frequency and voltage during transients. This contrasts with traditional GFL P/Q tracking controllers, which do not support the system during transients and in fact can often work to the detriment of grid synchronization and voltage/frequency regulation.
2. The GFM P/Q tracking controller tracks the commanded real and reactive power only if doing so does not cause the network to violate the specified voltage and frequency limits. This is in contrast with traditional GFL P/Q tracking controllers, which have been well documented to often cause the system to violate regulatory voltage and frequency specifications (especially at high penetration levels).

The P/Q tracking controller, like the baseline VOC, is based on the VOC approach. Unlike the baseline VOC, however, the GFM P/Q tracking controller requires an additional set of control loops to manage the P and Q tracking. The outer (P/Q tracking) loops operate on a slightly slower timescale than the inner (VOC) control loop. The result is that the GFM P/Q tracking controller's transient performance is dominated by the VOC loop (and therefore inherits VOC's synchronization and voltage/frequency regulation characteristics), whereas its slower (steady-state) performance is dominated by the P/Q tracking controller.

In the GFM P/Q tracking controller, synchronization and keeping the voltage and frequency within required limits are still the priority job. P/Q tracking occurs only once synchronization has been achieved and only as long as the voltage and frequency are within the limits. The simulated response of the controller is shown in Figure 12. We observed zero steady-state error and less than 1-second settling time, successfully meeting the metrics in Project Evaluation Criteria 1.3.b.

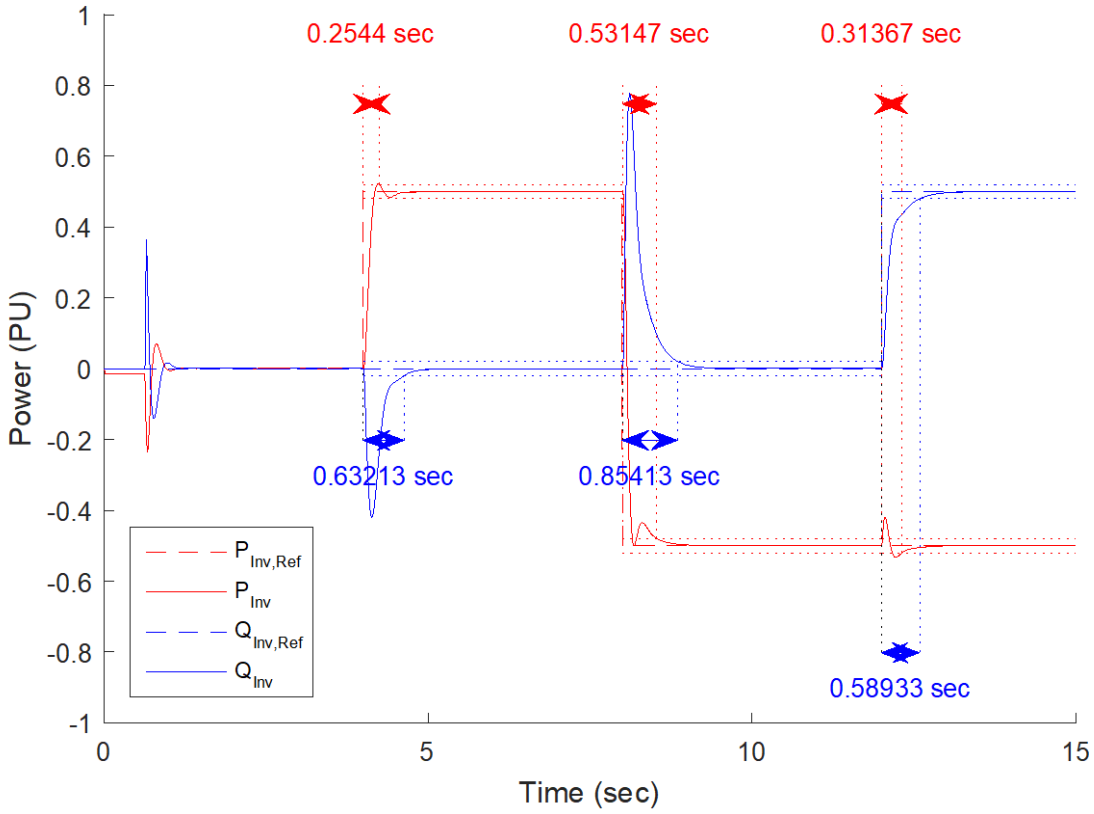

Figure 12. **Simulated response of the developed PQ tracking controller. The inverter is subjected to step changes in real and reactive power commands, denoted as P**inv,Ref**, and Q**inv,Ref**, respectively. As shown, the inverter successfully tracks the commands with zero error with a settling time of less than 1 second.**

3.3.3 Photovoltaic Inverter Controller with Maximum Power Point Tracking

The purpose of the third controller is to enable PV inverters to form an AC grid without the need for an explicit angle-tracking controller while concurrently performing maximum power point tracking (MPPT). In essence, our aim is to enable inverters to dynamically create an AC grid without a stiff source while extracting maximum PV energy. The key challenge is to ensure that the MPPT and GFM functionalities are carried out concurrently and are compatible with each other.

Our approach for this controller was built on the PQ tracking controller described. A control architecture consisting of an interconnected PQ tracking controller, DC-link voltage regulator, and MPPT loop was finalized. In particular, the developed architecture use an MPPT algorithm and controller to regulate the input stage DC-DC converter that interfaces the PV input. Subsequently, this DC power is delivered to the DC-AC converter with the aforementioned PQ tracking control. To ensure that the overall system functions seamlessly, the power command that is given to the DC-AC PQ tracking VOC is modulated to regulate the DC-link voltage. Consequently, the overall system achieves energy balance where the optimized power extracted to the PV is delivered to the DC-AC converter and the DC-AC converter is controlled with a GFM controller. Results in Figure 13 show satisfactory performance, where the power tracking

error is less than 5% and the settling time is less than 1 second, meeting Project Evaluation Criteria 1.3a.

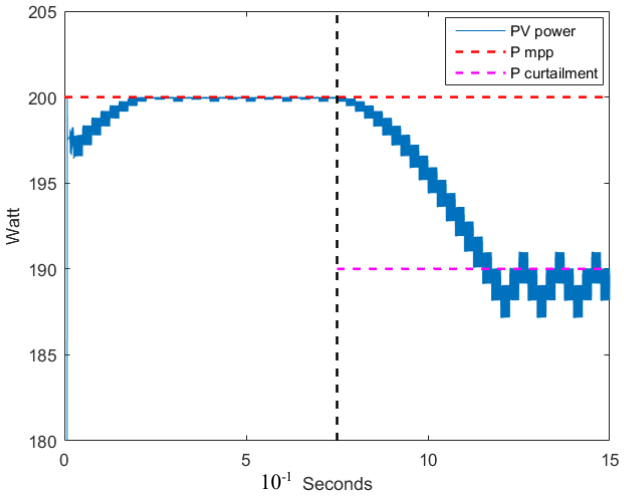

Figure 13. Simulation of PV inverter with GFM oscillator-based control. The plot depicts the power extracted from the PV module as would be seen with a PV microinverter. As shown, the power extracted from the PV successfully tracks the maximum power point with zero error. Further, the curtailment command, which is given at t = 0.75 second, is successfully tracked.

3.3.4 Customized Hardware Test Bed

To validate the control strategies developed under this task, we designed a custom power electronic inverter that is fully programmable and can execute any user-defined controller. A custom-designed solution was created to avoid any possible limitations with proprietary commercial designs and to maximize design flexibility. In addition to developing the inverter prototype, we designed a test bed to assess complex system performance. The test bed consists of five fully assembled inverter prototypes, secondary line impedances emulators, a radial line impedance emulator, a grid simulator, and a real-time HIL system. In this section, we provide a summary of the inverter prototype and the system test bed.

The printed circuit board layout of the single inverter prototype was completed, and a total of five fully assembled circuit boards were manufactured and constructed. Each inverter prototype was then interconnected with a user-programmable Texas Instruments C2000 F28335 DSP board and a BeagleBone board. The system was designed such that the Texas Instruments board executes any controller that has direct control over the power electronic semiconductor devices, and the BeagleBone board provides supervisory-level communications if needed (e.g., passing real and reactive power commands to the Texas Instruments board). One fully assembled unit is shown in Figure 14.

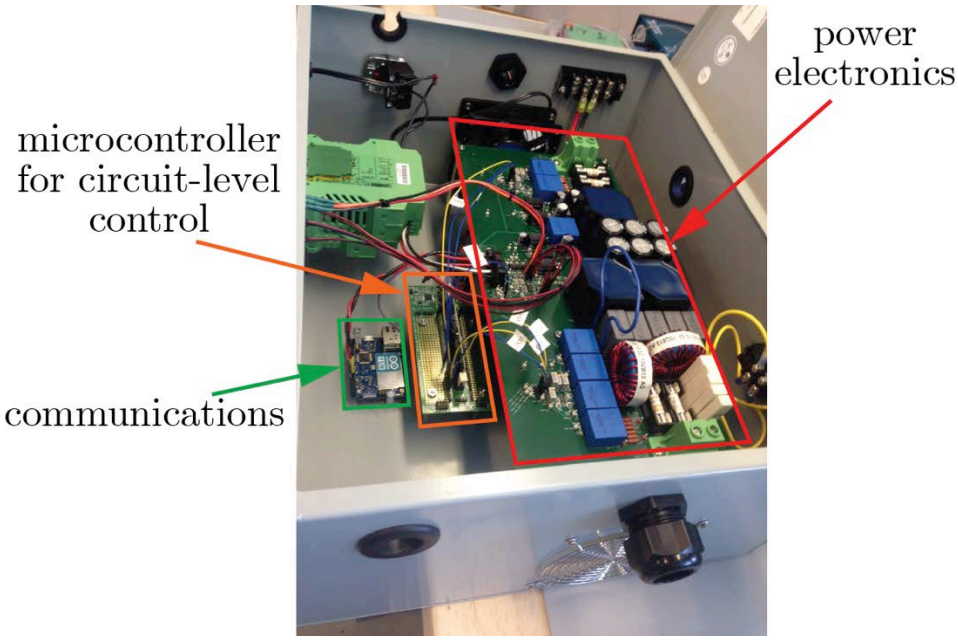

Figure 14. Photo of custom-designed inverter prototype. Developed controllers are executed on the microcontroller board, and information exchanges between the inverter unit and user are carried out with the communications board. *Photo by NREL*

The design of the system-level test bed is complete, as depicted in in Figure 15. As shown, the test bed consists of not only the inverter prototypes as described but also line impedances, a grid simulator, communications, and a laptop. In this setting, the line impedance emulators are under construction, with hardware inductors and resistors where the parameters of these components have been selected to correspond to typical impedances observed in realistic feeders. A grid-simulator will be used to emulate the point of common coupling that interfaces with the remaining system. For more complex experiments, the grid simulator will be programmed to execute various profiles and possibly even emulate machine inertia. Multiple units of these grid simulators already exist within NREL's Energy Systems Integration Facility laboratories. Note that the images in Figure 15 correspond to photos of the actual hardware that has been built. These components have successfully been interconnected as a system.

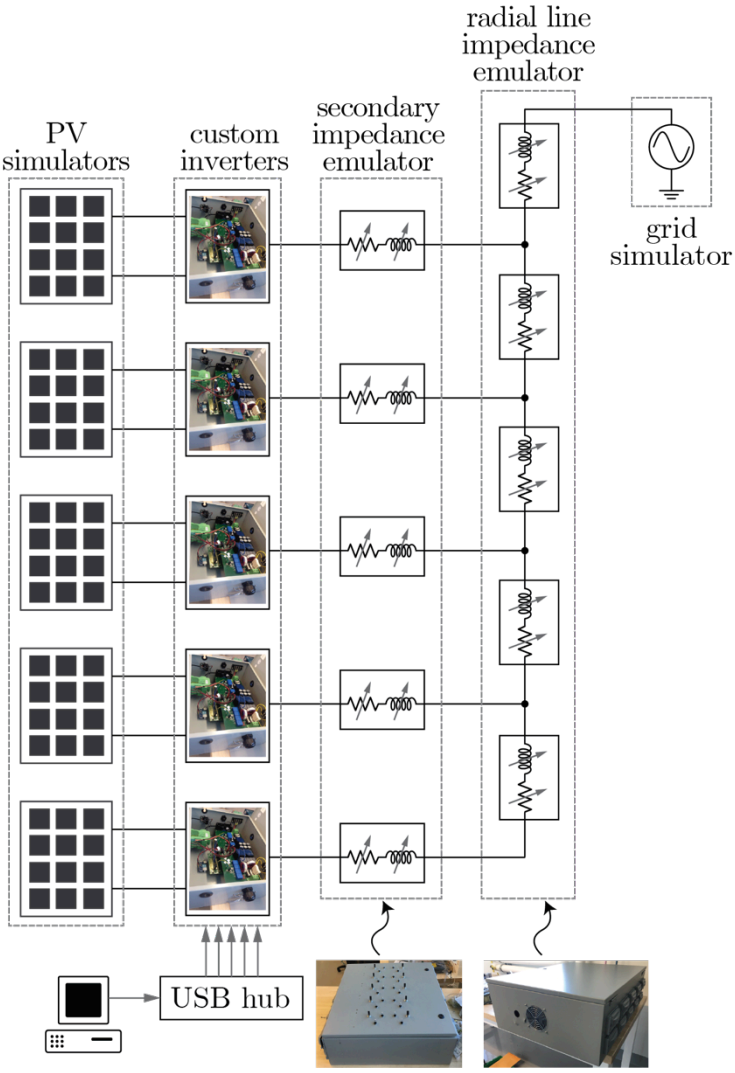

Figure 15. Diagram of completed multi-inverter test bed. The five inverter prototypes and radial line impedance emulators have been fully constructed. *Photos by NREL*

3.3.5 Compare the Performance of the Proposed Oscillator-Based Controller to Droop Control

At this time, the most widely used GFM inverter control strategy is known as droop control. Given the well-established nature of droop control and its wide adoption in the power electronics community, it acts as the main competing control strategy to VOC. The purpose of this task is to delineate the differences in performance between VOC and droop control so that power electronics practitioners can understand the value of new strategies such as VOC. The following results were published in the 2017 Workshop on Modeling and Control of Power Electronics conference under a paper titled "Comparison of Virtual Oscillator and Droop Control."

Droop control draws inspiration from synchronous machine networks by programming a linear relationship between steady-state real power versus frequency and steady-state reactive power versus voltage. Given that real and reactive power are phasor quantities that are not well defined in real time, droop controllers typically use multiplicative operations in conjunction with low-

pass filters on the current and voltage measurements to calculate such quantities. Because these filters must suppress low-frequency AC harmonics, they typically have low cutoff frequencies that ultimately impede droop controller bandwidth. In contrast, the proposed VOC are time-domain controllers that act on real-time measurements and provide an instantaneous response to changing system conditions. Although VOC can provide enhanced speed and bandwidth, it can also be engineered to exhibit the same droop-like characteristics in steady state. So, although VOC and droop control can yield similar steady-state characteristics, their dynamic performance can differ markedly. In this work, we analyzed and quantified the performance gains with VOC and validated the analysis experimentally.

Here, we state the main conclusions from the conference paper (Johnson et. al. 2017), and the interested reader can read the full paper for details. First, we developed an analytical model of the droop-controlled and virtual oscillator-controlled inverters. Given that both the droop and VOC dynamic system models are nonlinear, both models were linearized so that their eigenvalues could be computed. Here, the eigenvalues were computed because they are useful in characterizing the speed and time-domain response of both controllers. Results are shown in Figure 16, which shows that droop has a more sluggish and oscillatory response than the VOC.

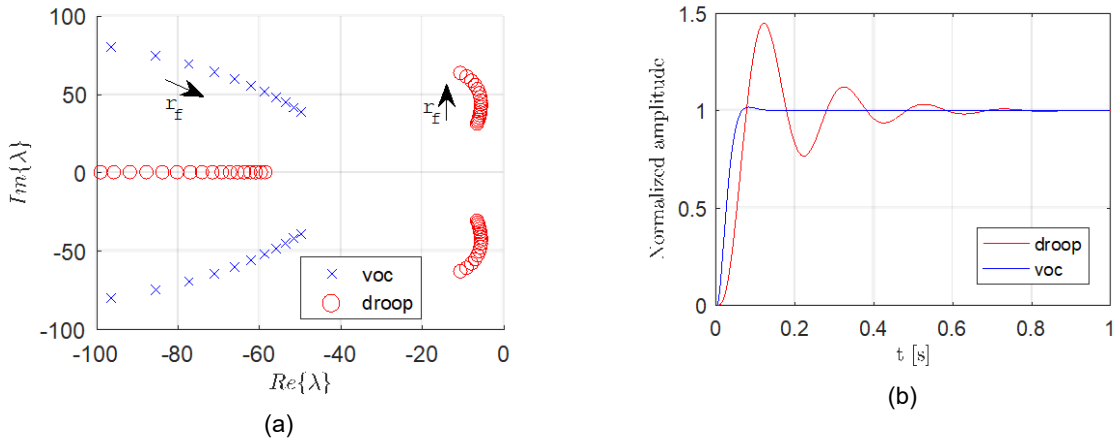

Figure 16. (a) Eigenvalues of the droop and VOC systems as the filter resistance is increased. (b) Step response of the transfer functions we obtained from the linearized droop and VOC models. Note that the eigenvalues and time-domain simulation both indicate that droop has a more sluggish and oscillatory response than the VOC.

Subsequently, the test bed and inverter hardware were used to experimentally validate the eigenvalue analysis and show that VOC exhibits superior speed and performance. In particular, the setup was configured such that it consisted of three 1-kVA parallel inverters operated at 120 V in an islanded configuration with a resistive load. The results in Figure 17 show the measured results for two multi-inverter experiments, where one experiment shows the response with VOC and the other with droop. Upon close inspection of the results, it is evident that VOC reaches steady state approximately eight times faster after a disturbance.

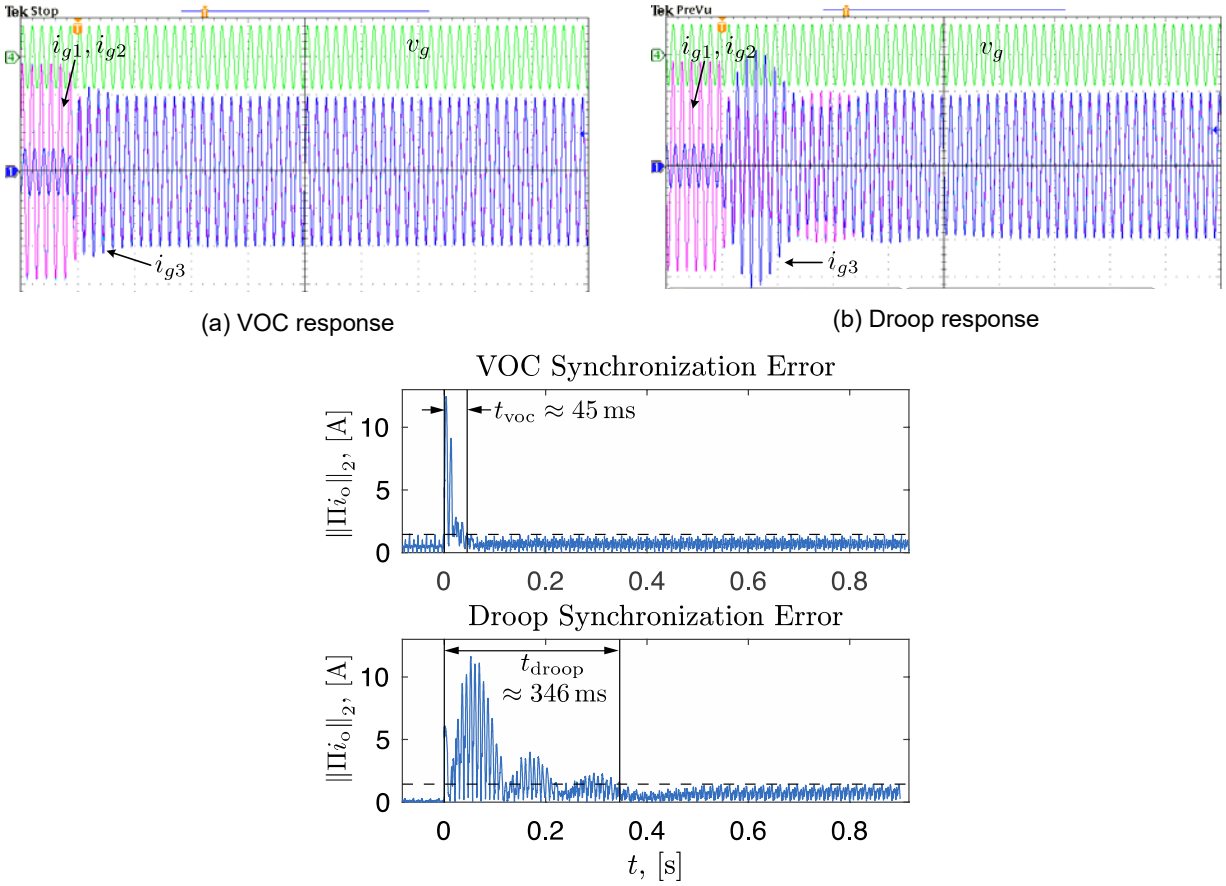

(a) VOC response

(b) Droop response

(C) Measured synchronization error

Figure 17. Addition of Inverter 3 when inverters 1 and 2 are supplying a 1-kW load. In each plot, the timescale is 100 ms/div, 2A/div for the currents and 100 V/div for the measured voltage. Figures (a) and (b) show the response of the inverter system with VOC and droop control, respectively. Here, the superior speed and transient response of VOC is evident. To obtain a more precise estimate of the speed difference, we plot the synchronization error from (a) and (b) in (c), where t_{voc} and t_{droop} indicate the time it takes for each system to synchronize. Using the measured synchronization times in (c), we estimate that VOC is approximately 8 times faster than droop control for this case.

3.3.6 Characterizing the Performance of Grid-Forming Controllers Under Varying Levels of Emulated Inertia

The experimental setup shown in Figure 18 was assembled, the HIL code for the machine model was completed, and the mixed inverter-machine PHIL experiment was conducted. Here, the machine was emulated in PHIL, and the inverters were actual hardware. We validated our approach to devise so-called "variable inertia" experiments. Our technique for variable inertia emulation is based on scaling the measurements from the inverter hardware that are subsequently processed by the HIL machine model. By scaling the measured inverter current by some gain, k_i, we are in effect changing the size of the inverter that the machine model is coupled to (although the actual hardware is fixed in size). In other words, by scaling the measurements properly, we are recreating the scenario of the tipping point analysis in Task 2.1, where we scale the rating of the inverter with respect to the machine rating. The main difference here is that the physical

inverter hardware is fixed, and we are merely using measurement scaling to achieve the same effect in a closed-loop HIL experiment. Referring to the experimental results in Figure 19 and Figure 20, it is evident that the emulated machine performs as anticipated—in Figure 19, we show the dynamic response under a step change in inverter power output, and in Figure 20, we show that the emulated machine behaves as expected in steady-state.

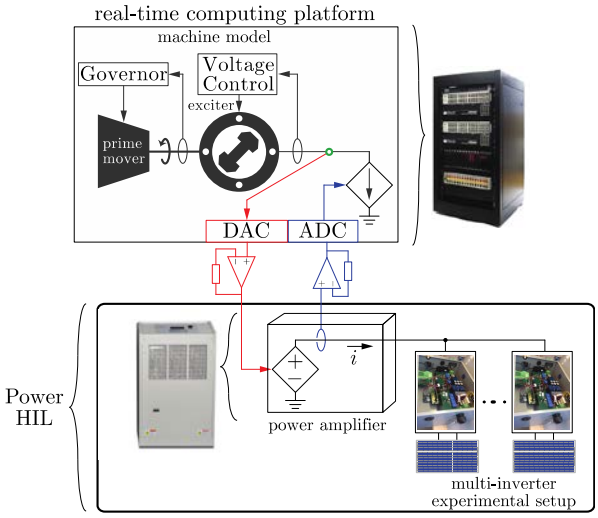

Figure 18. Multi-inverter setup with PHIL for variable inertia emulation. *Photos by NREL*

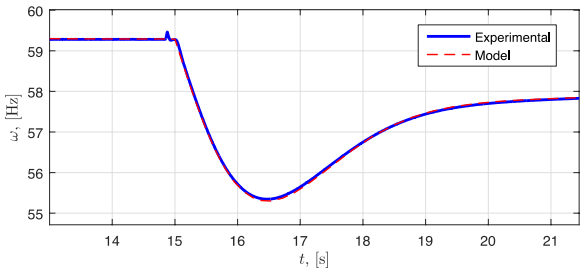

Figure 19. Dynamic response under a 25% to 75% load step

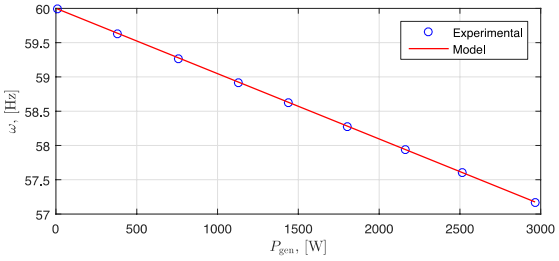

Figure 20. Steady-state speed droop

3.4 Develop Scalable Inverter Model (Associated with Tasks 2.1, 2.2, and 3.1)

To enable the analysis of systems with large numbers of inverters, a key task is to develop a model to represent a collection of inverters. In this section, we present an aggregation methodology that has been developed to address this issue. More details are reported in Purba et. al. (2017).

3.4.1 Scalable Grid-Following Inverter Model

Building on the scalable, three-phase inverter model shown in Figure 21, the methodology is to combine multiple inverters with different power ratings into a single equivalent inverter. This approach greatly reduces the number of states in the system and simplifies the stability analysis.

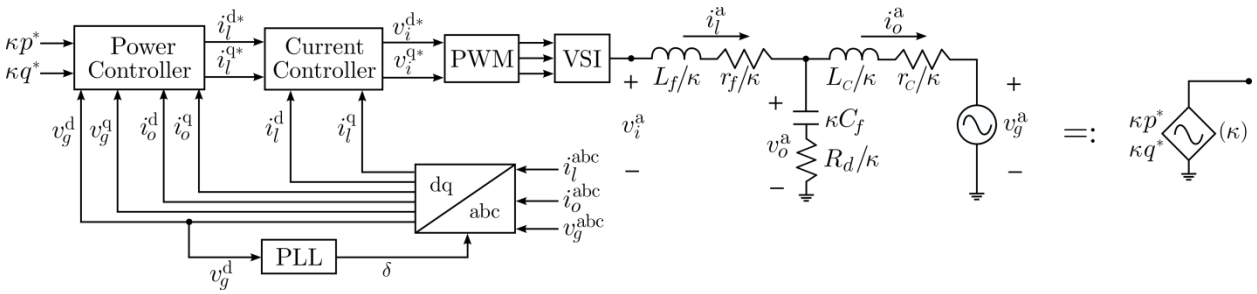

Figure 21. Block diagram of the scalable three-phase inverter. One phase is depicted on the physical side for simplicity. Signals superscripted by d and q are DC; otherwise, they are AC.

Following Figure 21, a single scaling parameter, κ, that represents the power rating of the inverter is introduced. The different parameters of the inverter should be scaled as:

- LCL filter: $\mathrm{L_f}/\kappa, \mathrm{r_f}/\kappa, \kappa C_f, R_d/\kappa, L_c/\kappa, r_c/\kappa$
- Power controller: $\mathrm{k}_P^p, \mathrm{k}_Q^q, \mathrm{k}_P^i, \mathrm{k}_Q^i$
- Current controller: $\mathrm{k}_{id}^p/\kappa, \mathrm{k}_{iq}^p/\kappa, \mathrm{k}_{id}^i/\kappa, \mathrm{k}_{iq}^i/\kappa$
- PLL: $\mathrm{k}_{PLL}^p, \mathrm{k}_{PLL}^i$.$\mathrm{L_f}/\kappa, \mathrm{r_f}/\kappa, \kappa\mathrm{C_f}, \mathrm{R_d}/\kappa, \mathrm{L_c}/\kappa, \mathrm{r_c}/\kappa,$

The state and input vectors of the inverter are:

$$\underline{x} = \left[i_l^{\mathrm{dq}}, i_o^{\mathrm{dq}}, v_o^{\mathrm{dq}}, \gamma^{\mathrm{dq}}, p_{\mathrm{avg}}, q_{\mathrm{avg}}, \phi_p, \phi_q, v_{\mathrm{PLL}}, \phi_{\mathrm{PLL}}, \delta\right]^{\mathrm{T}}, \ \underline{u}_1 = [p^*, q^*]^{\mathrm{T}}, \ \underline{u}_2 = \left[v_g^{\mathrm{a}}, v_g^{\mathrm{b}}, v_g^{\mathrm{c}}\right]^{\mathrm{T}}.$$

Let $\underline{x}^s$ denote the state vector of the scaled inverter, and $\underline{\kappa}$ is a scaling vector defined as $[\kappa\mathbb{1}_2^{\mathrm{T}}, \kappa\mathbb{1}_2^{\mathrm{T}}, \mathbb{1}_2^{\mathrm{T}}, \kappa\mathbb{1}_2^{\mathrm{T}}, \kappa, \kappa, \kappa, \kappa, 1, 1, 1]^{\mathrm{T}}$, where $\mathbb{1}_n$ denotes a vector of all ones with length n. Suppose that the controls are related as $\underline{u}_1^s = \kappa\underline{u}_1, \underline{u}_2^s = \underline{u}_s$, and suppose that the initial conditions are chosen without loss of generality such that they satisfy $\underline{x}^s(t_0) = \mathrm{diag}(\underline{\kappa})\underline{x}(t_0)$, where $\mathrm{diag}(\underline{\kappa})$ denotes a diagonal matrix with its diagonal entries to be the entries of $\underline{\kappa}$. Then, for every $t \geq t_0$, we have:

$$\underline{x}^s(t) = \mathrm{diag}(\underline{\kappa})\underline{x}(t).$$

This result means that the states of the scaled inverter are directly proportional to the states of the original inverter.

Now consider n scaled inverters with scaling factors of $\kappa_1 \ldots \kappa_n$ connected in parallel to the point of common coupling, as illustrated in Figure

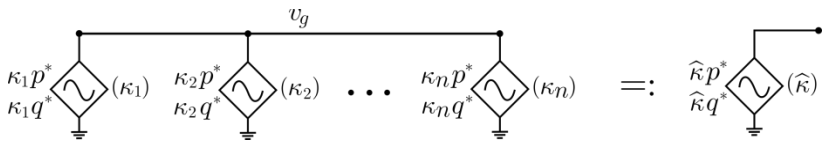

Figure 22. Shorthand diagram of n inverters connected in parallel

Let $\hat{\kappa}$ denote the sum of the scaling factors of the parallel connected inverters, i.e., $\hat{\kappa} = \sum_{\ell=1}^{n} \kappa_\ell$. Let the equivalent inverter be a scaled inverter with scaling factor of $\hat{\kappa}$, and its state vector is denoted by $\underline{x}^e$. Suppose the control inputs and initial conditions of the individual and equivalent inverters satisfy the same conditions as for the scaled inverter. Then, for $t \geq t_0$, the current out of the equivalent inverter is the sum of the output current of individual inverters, i.e.:

$$i_o^{\mathrm{dq}e}(t) = \sum_{\ell=1}^{n} i_{o\ell}^{\mathrm{dq}}(t).$$

Consequently, the output power of the equivalent inverter is the total output power of all the inverters. This result (provided that the general topological assumptions hold) demonstrates that an arbitrary number of inverters can be modeled as a scaled, single inverter, thus enormously simplifying the analysis of systems with large number of inverters. Figure 23 graphically summarizes these results.

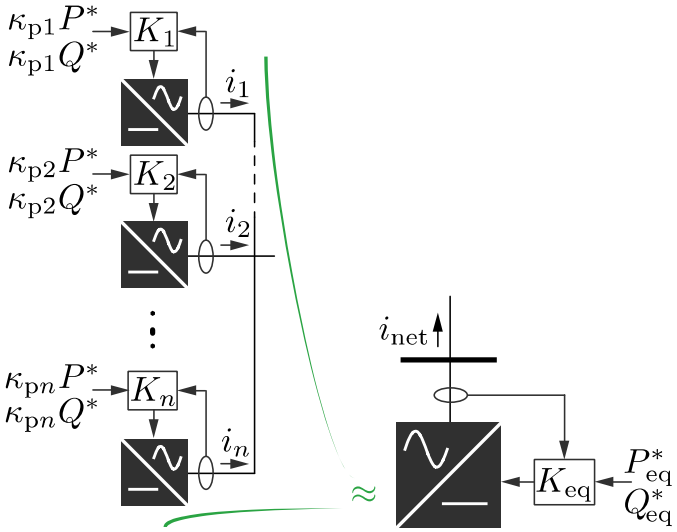

Figure 23. An arbitrary number of inverters can be represented as a single inverter using scaling parameter Keq=κ.

Time-domain simulations using full nonlinear inverter models have been carried out to confirm these findings. Four 500-W grid-connected inverters are simulated, along with the aggregated model obtained following the proposed methodology. The inverters are turned on at t=0 producing their full 2-kW load; at t=0.5 second, a step change in the active power command, p^*, from 500 W to 400 W occurs.

Figures 24 and 25 show the output current of the inverter and the output active power. The aggregated model fully captures the dynamics of the four inverters connected in parallel, thus confirming the validity of the proposed method.

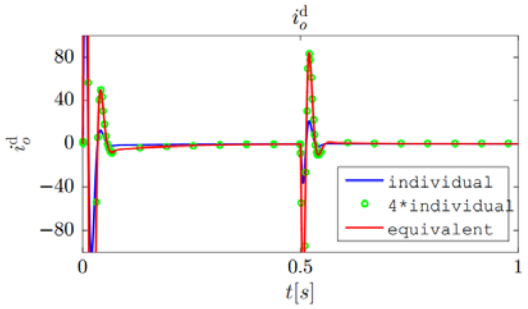

Figure 24. Output current

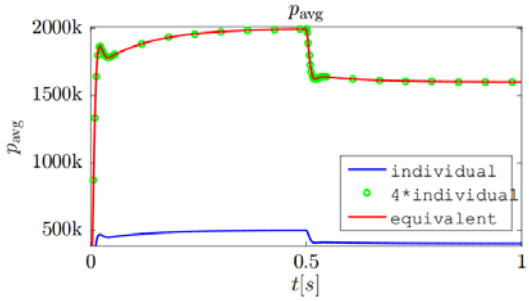

Figure 25. Capacitor voltage

To further substantiate our approach, we conducted a new set of experiments where three inverters were connected to a stiff grid. The inverters were subjected to a set of dynamic conditions, and the output current of each inverter and at the grid point of interconnection was recorded. Subsequently, we ran a simulation of one equivalent inverter subjected to the same set of transients. Figure 26 shows that the model of the single equivalent inverter matches the experimental results with three distinct hardware inverters. In this experiment, the inverters experienced a step change in the power output from 0 W to 500 W at t = 3.2 seconds. The waveforms illustrate that the measurements and simulated equivalent inverter show a remarkably close match. This new result was reported in Purba et. al. (2018).

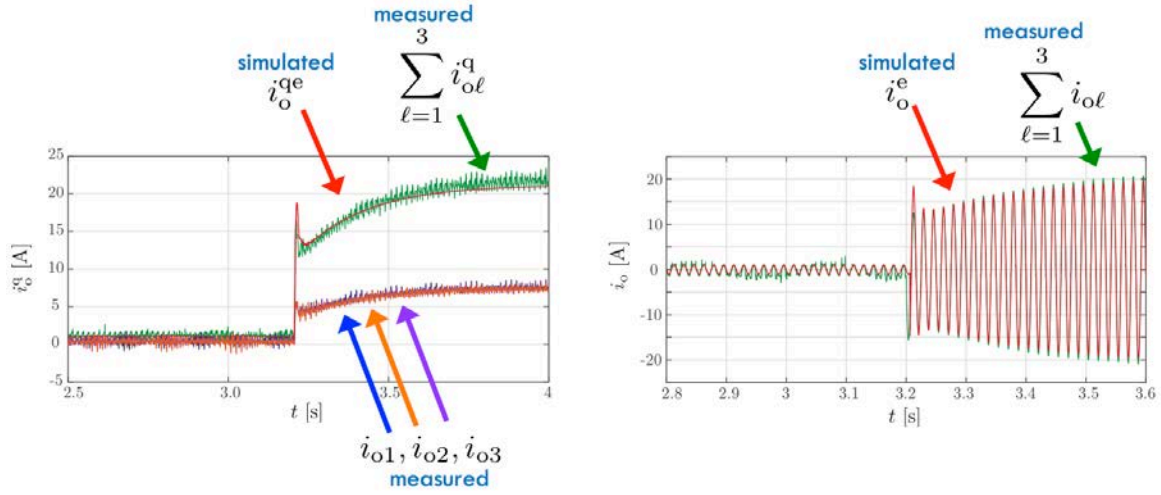

Figure 26. Response of the hardware test bed consisting of three parallel-connected inverters and a simulated equivalent inverter (red curve) after receiving a step change in power output. Results show that the aggregated equivalent model closely matches the measured result.

To extend our foundational results to more realistic feeder systems, we created a framework for increasingly complex network settings. To consider the network, we developed an approach that we call network-cognizant aggregation because it properly accounts for network impacts. The crux of the approach is the development of a clustering method that depends on feeder voltages. In summary, inverters that are electrically close to one another and experience similar voltages can be clustered together and represented as an aggregated equivalent. Further, the accuracy of

the aggregated feeder equivalent depends on the number of clusters, where a larger number of clusters gives higher accuracy at the expense of a more computationally intensive model.

We developed an algorithm based on the K-means clustering method. To summarize, this framework accounts for the voltages across a given network and clusters inverters that are electrically close to one another and experience similar voltages. The example in Figure 27 shows the result of the clustering algorithm when applied to the Institute of Electric and Electronics Engineers (IEEE) 37-us feeder system. Once the clusters are obtained, the inverters within each group are transferred to a common bus with virtual transformers and then aggregated according to the approach established described in the beginning of this section. Note that the reduced-order feeder model we obtain accounts for all internal inverter control dynamics (e.g., PLL, current control) and is valid during transient conditions.

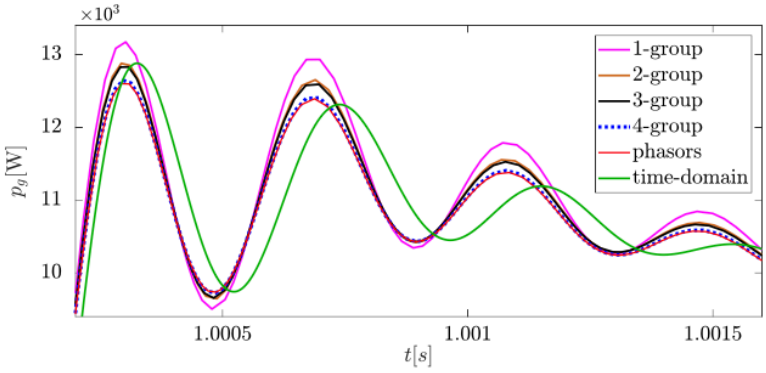

Figure 27. Time-domain waveform for the net power generated by the feeder system for varying numbers of clusters. As shown, the system behavior becomes closer to the phasors model with larger numbers of clusters.

3.4.2 Scalable Grid-Forming Inverter Model

In this section, we discuss an aggregated VOC model that can represent many VOC inverters. We showed that if the control and physical parameters of each inverter controlled with VOC in a parallel system adhere to a set of scaling laws (Figure 28(a)), then the output current of a multi-inverter system can be modeled exactly with one aggregated equivalent inverter model (Figure 28(b)). More details are reported in Khan et. al. (2018b).

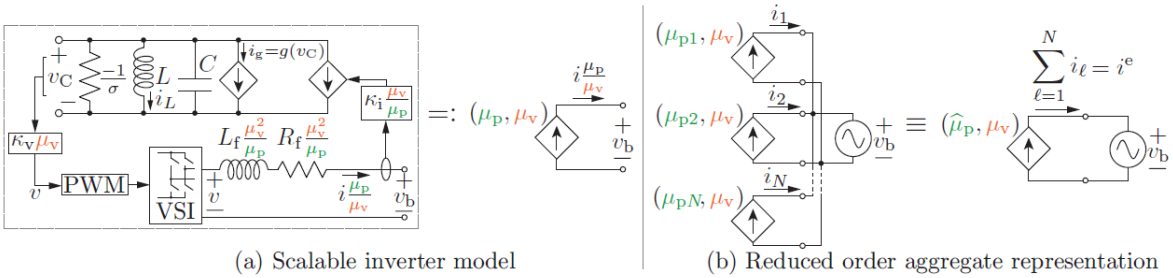

Figure 28. (a) Diagram of the scalable model for a single inverter with VOC, where μp and μv are the power and voltage scaling factors, respectively. (b) A system of N parallel virtual oscillator-controlled inverters with heterogeneous power ratings can be modeled equivalently as one reduced-order aggregated inverter.

The proposed framework is validated by comparing measurements from a multi-inverter hardware setup with heterogeneous power ratings to a reduced-order simulation of the system. The experimental results are shown in Figure 29, where we provide the measured waveforms alongside the simulated waveforms of the aggregate inverter model during load step changes. Evidently, the net current delivered by the multi-inverter hardware setup can be modeled with the complexity of a single inverter equivalent, thus giving us a factor of 1/N savings in model order.

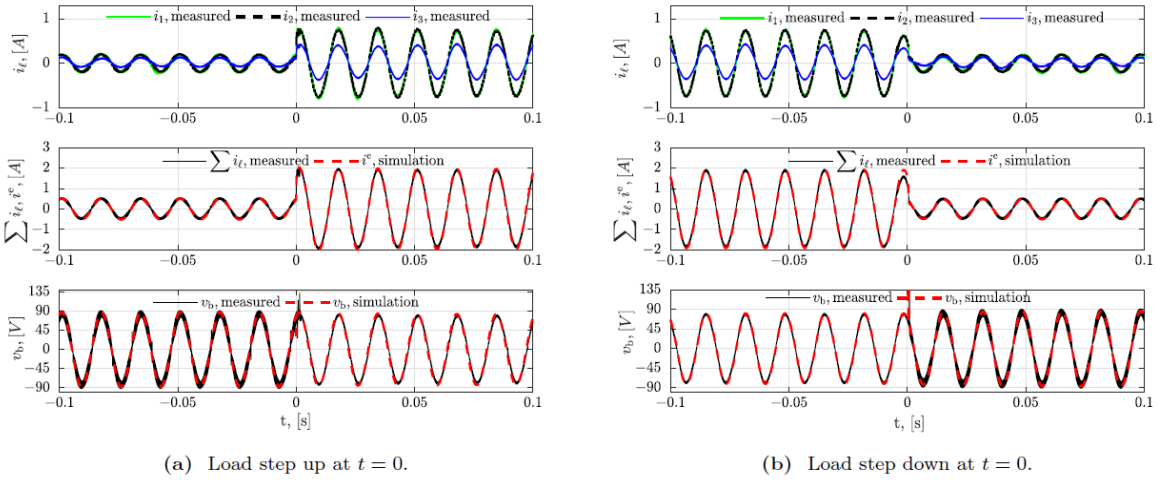

(a) Load step up at $t = 0$. (b) Load step down at $t = 0$.

Figure 29. Comparison of measurements obtained for a multi-inverter system to simulated waveforms for the reduced-order aggregate inverter model. Waveforms during a load step-up and step-down are shown in (a) and (b), respectively. From top to bottom, each plot shows the measured currents delivered by each of the three inverters, the measured net current and the aggregate equivalent current overlaid on each other, and the bus voltage of the experimental and simulated systems.

3.5 Tipping Point Analysis for Grid-Following Inverters (Associated with Tasks 1,1, 2.1, and 3.1)

To characterize the tipping point of coupled inverter-machine systems, we started with an elementary single-machine, single-inverter model. Although this model appears simple, we found that it is a good starting point to understand the stability properties of the systems. After

analyzing the single-machine, single-inverter model, we extended the tipping point analysis to multi-unit systems.

3.5.1 Single-Machine, Single-Inverter System

The results on the tipping point of the single-machine, single-inverter system are reported in a paper titled "Stability Assessment of a System Comprising a Single Machine and Inverter with Scalable Ratings," submitted to the North American Power Symposium for publication in summer 2017.

For brevity, we briefly state the finalized results of this paper and subsequently describe next steps for multi-inverter, multi-machine networks. Using the scalable inverter model described for the aggregation results, we studied the case where one large inverter with a "scalable" power rating is interfaced to a prototypical synchronous machine. Here, the scalable model is key to resolving the large disparity in size between typical machines and inverters. For instance, a typical power plant machine is rated for hundreds of MVA, whereas inverters are generally no larger than hundreds of KVA; hence, it would take thousands of inverters to be on par with the size of a single machine. Rather than model 1,000 distinct inverters, however, we rely on the aggregated representation, where the collection of inverters is modeled as an aggregated equivalent. As illustrated in Figure 30, we use the parameter κ_p as a "knob" to tune the power rating of the scalable inverter model; hence, by varying κ_p from a small initial value to a large value, we can evaluate the system under an increasing level of inverter penetration. Here, we define the inverter penetration level as the ratio $\frac{P_i}{P_i+P_m}$, where P_i and P_m are the inverter and the synchronous machine power ratings. To assess stability, we linearize the system at each penetration level and assess the eigenvalues at each point. If any eigenvalues in the complex vector λ have positive real parts, then the system is unstable.

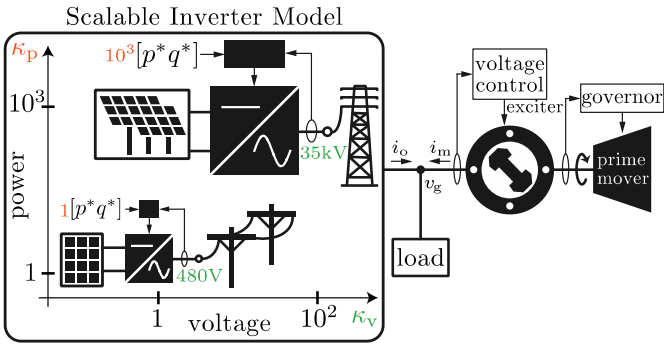

Figure 30. Model of a single-machine, single-inverter system, where the power and voltage ratings of the inverter are scalable. This model is an abstraction of low-inertia systems and is intended to assess possibly unforeseen dynamic interactions between machines and inverters.

The plots in Figure 31 and Figure 32 summarize the main results of our study, where the inverter model is based on the inverter hardware used in the NREL experiments, and the machine parameters are from a widely used textbook model. As shown in Figure 30, system stability is maintained for penetration levels less than approximately 45%, but stability is lost with higher penetration levels. To discern the root cause of the problem, we performed a detailed analysis where various inverter and machine subsystems were either bypassed or neglected. Ultimately, we found that if the machine automatic voltage regulator was bypassed (assuming voltage

control is achieved instantaneously), then the instability was eliminated (See Figure 32). This observation indicates that the machine voltage control loop has a destabilizing interaction with the inverter controllers. We believe this is an important observation that could possibly inform system operators and inverter manufacturers on potential issues that are so far unforeseen in existing literature.

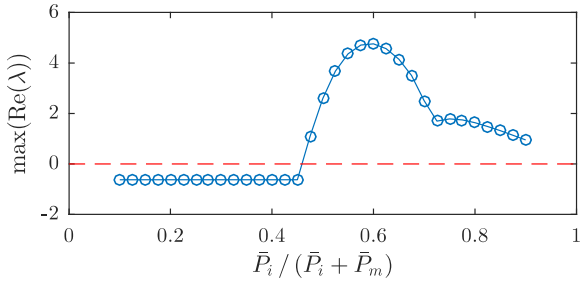

Figure 31. Small-signal stability is ensured for penetration levels approaching 45% with the full detailed system model.

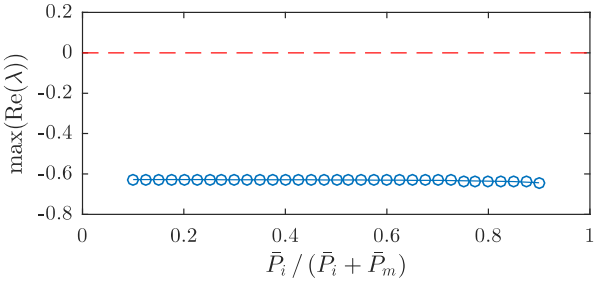

Figure 32. Bypassing the machine automatic voltage regulator and exciter circuit significantly improves the stability margins.

3.5.2 Multi-Machine, Multi-Inverter System

We extended the multi-machine, multi-inverter tipping point analysis to the IEEE 39-bus system. This system is generally representative of the New England 345-kV system, which provides a more realistic test bed to study the stability properties of combined inverter and machine systems. Simulations show similar results to the smaller system previously studied, where the system becomes unstable as the inverter penetration level increases.

To study a more realistic system, we use the IEEE 39-bus system. There are 10 generators in the system. Bus 39 represents the connection with the rest of the Eastern Interconnection. In this study, this is modeled as a large synchronous generator and a large load. In this simulation, we replace the synchronous machines with inverters of the same capacity one at a time to represent different inverter penetration levels. More specifically, we start with the original 39-bus system. Then we replace the generator at Bus 30 with an inverter with the same capacity. Next, we replace the generation at Bus 31 with an inverter with the same capacity. This provides an increasing inverter penetration level. One benefit of this approach is that the system line parameters remain compatible because the power flow does not change as we replace the generators with inverters. The results are show in Figure 33.

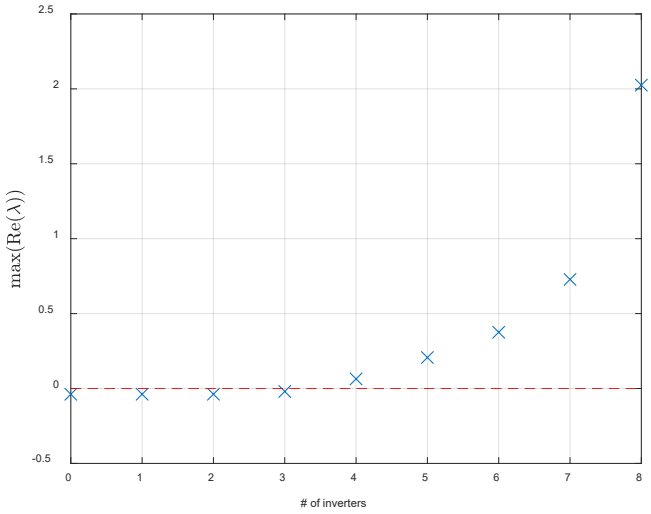

Figure 33. Small-signal stability results for the IEEE 39-bus system. The x-axis indicates how many machines are replaced with inverters. The y-axis indicates the real part of the largest eigenvalue; the system is stable when this value is negative, and it is unstable when this value is positive.

We observed that the system becomes unstable as we replace four generators with inverters. The corresponding power capacity replaced by the inverters is 35% of the total power capacity of the system. Similar to the single-unit case, the tipping point depends on system parameters, including controller gains and filter parameters.

3.6 Tipping Point Analysis for Grid-Forming Inverters (Associated with Tasks 2.2 and 3.1)

In this section, we present the tipping point analysis for the VOC GFM inverters. Similar to the GFL case, we start with a single-inverter, single-machine system and extend it to multi-unit systems.

3.6.1 Single-Machine, Single-Inverter System

The results discussed in this section are reported in Khan et. al. (2018a). The first step is to develop an aggregated VOC model that can represent many VOC inverters. We showed that if the control and physical parameters of each inverter controlled with VOC in a parallel system adhere to a set of scaling laws, then the output current of a multi-inverter system can be modeled exactly with one aggregated equivalent inverter model.

Next, we leverage this aggregated VOC model to analyze the small-signal stability of the same single-inverter, single-machine model in the GFL case. With some algebraic manipulation, the system dynamics can be written as an ordinary differential equation:

$$\dot{x} = f(x, u)$$

We then linearize the system around an equilibrium point, and we calculate the eigenvalues to determine the stability of the system. We evaluate the stability at different penetration levels. The results for the default case (parameters chosen for 5% droop slope; more details are discussed in

Khan et. al. (2018a)) are shown as the black line in Figure 34. We observe that the system becomes unstable as we increase the inverter penetration level. The tipping point is near 50% in this case.

To study the impact of the inverter parameters, we performed a sensitivity analysis. We observe that the inverter reactive power droop slopes have a significant impact on the system stability; this is shown in Figure 34. By carefully choosing the inverter parameters (for example, droop slopes), the system can remain stable with an inverter penetration level greater than 90%.

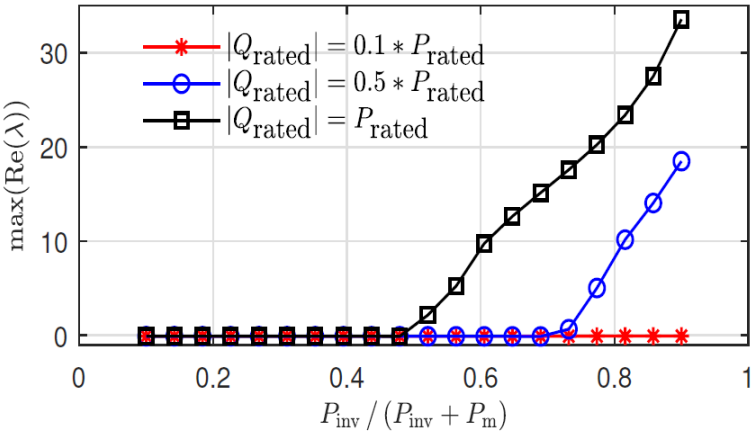

Figure 34. Impacts of reactive power droop curve

3.6.2 Multi-Machine, Multi-Inverter System

Similar to the GFL case, we extended the multi-machine, multi-inverter tipping point analysis to the IEEE 39-bus system. Results show that with the careful selection of system parameters (such as droop slopes and filter parameters), the system can remain stable across all inverter penetration levels, as shown in Figure 35.

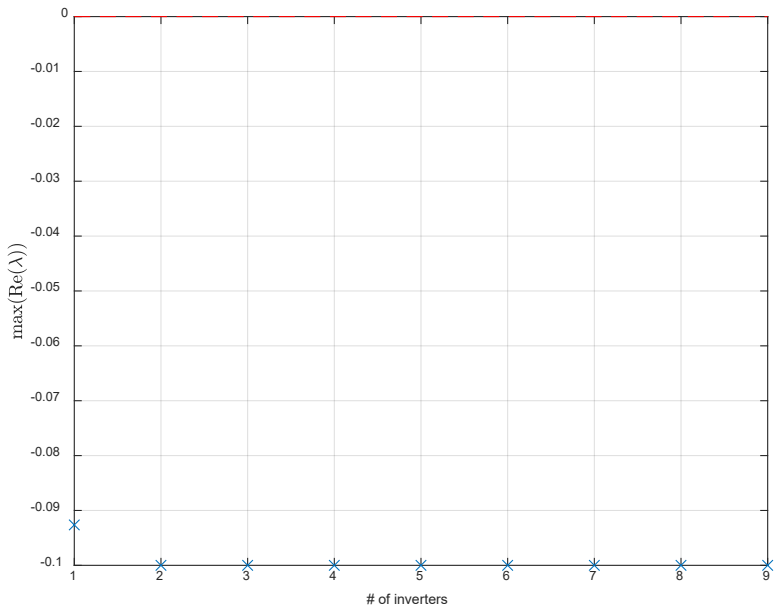

Figure 35. Small-signal stability results for the IEEE 39-bus system. The x-axis indicates how many machines are replaced with inverters. The y-axis indicates the real part of the largest eigenvalue; the system is stable when this value is negative, and it is unstable when this value is positive. Transient Behavior Modeling for Grid-Following Inverters (Associated with Task 2.1)

In this effort, we aim to analyze the dynamic performance of solar power stations in bulk power systems during transmission faults. Results in this section are reported in Pico and Johnson (2019). Transmission faults caused by recent wildfires in California induced the disconnection of utility-scale converters in PV power plants. Postmortem investigations reported that tripping commands were caused by PLLs and DC-side dynamics, which are typically unmodeled in transient stability studies. Because existing simulation packages rely on simplified models that neglect these dynamics, they have limited capability to predict converter behavior during faults. To address this shortcoming, we set forth a positive-sequence model for PV power plants that is derived from physics and controls first principles. As shown on utility-scale three-phase converters, the model includes PLLs, DC-side dynamics, and closed-loop controllers. Instances of the developed model are integrated into an illustrative power system that also contains conventional generators. Numerical simulations of the obtained multi-machine, multi-converter power system are assessed via a suitable set of stability and performance metrics.

To comprehensively predict the transient response of PV power plants while avoiding burdensome computations of EMT studies, we propose incorporating higher fidelity models into positive-sequence transient simulations. We focus on the most used three-phase converter structure in industry, which comprises a single DC-to-AC conversion stage. We also leverage the artifact that synchronous and converter-based generation act as positive-sequence sources and that asymmetric transmission faults can be modeled in the positive-sequence domain. To ascertain transient performance from simulations, we look beyond rotor-angle stability and assess the voltage ride-through capability of converter-based generation as mandated by grid codes. This manuscript specifically provides the following contributions: (1) a voltage behind-reactance model of a PV power plant that is derived from circuit laws and expressed in a

reference frame whose angle and speed is provided by its PLL (e.g., see Figure 36); (2) an iterative scheme with proof of convergence to seamlessly incorporate the nonlinear representation of a PV array and DC-link into transient stability studies; and (3) a set of stability and performance metrics to assess numerical simulations and ascertain whether conventional and converter-based assets are compromised during faults (e.g., see Figure 37). The proposed modeling framework and assessment metrics align with state-of-the-art reliability guidelines (NERC 2018).

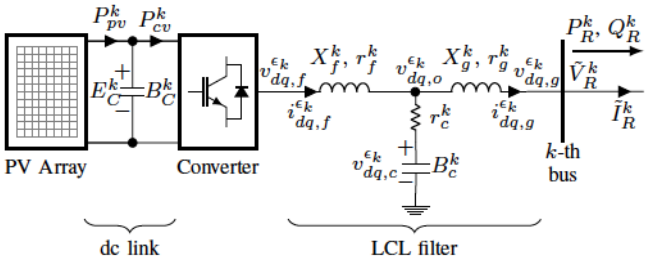

Figure 36. Aggregated representation of a PV power plant

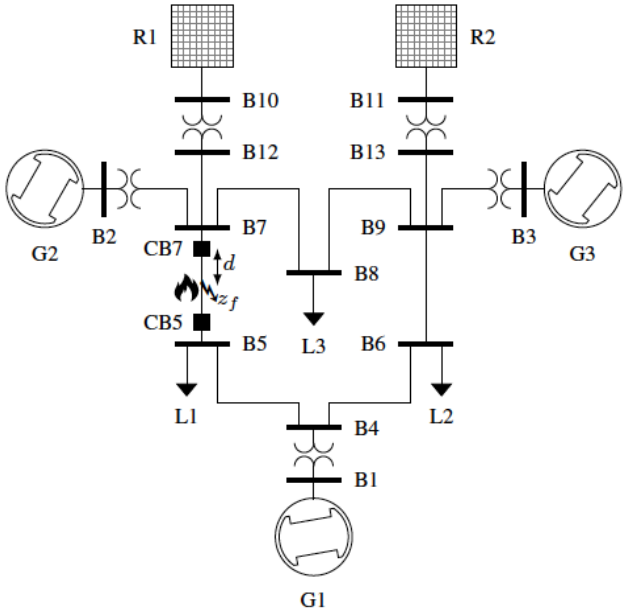

Figure 37. Modified Western System Coordinating Council nine-bus power system with PV power plants

3.7 Hardware Demonstration with SunPower Micro-Inverters

This effort expands prior experiments and models of GFM controllers to increasingly complex and realistic settings using 20 SunPower microinverters. First, the team successfully implemented VOC on SunPower's current generation microinverter. A 10-microinverter test bed was created. All 10 microinverters worked to generate a stable grid by synchronizing to each other and sharing load power without communication. The test bed demonstrated fast dynamic response capable of supporting resistive load step changes with minimal disturbance to the system voltage. Next, the test bed was expanded to incorporate a total of 20 microinverters. The

test bed represents a small microgrid that incorporates 10 VOC microinverters (GFM) and 10 conventional microinverters(GFL) to characterize their compatibility and evaluate system performance. In addition to the resistive load, the team introduced reactive components to test the system operation with reactive loads.

The hardware of the 20-microinverter test was assembled at NREL. First, the 10-GFM microinverter cabinet created in Fiscal Year 2017 was repurposed. The AC wiring was rearranged to allow for the inclusion of inductive components. Also, the resistive load bank was modified with the addition of a parallel capacitor that could be switched in and out of the circuit with a power relay. A second (GFL) cabinet was designed to have 10 GFL microinverters and inductive components. Upon completion of the 20-microinverter test bed, the experimental test sequence was finalized. Python functions were developed to automate portions of the test sequence. The execution of the test sequence yielded voltage and current data that served to evaluate the system performance under both resistive and reactive load transients and steady-state operation.

3.7.1 Test Bed Setup

Figure 338 illustrates a simplified electrical diagram of the 20-microinverter test bed. Microinverters number 1 through 10 are GFM microinverters operated with the VOC. Those 10 microinverters are divided into two clusters of five units: microinverters 1–5 and microinverters 6–10. Between the two clusters of five microinverters, an inductor (L1) is installed in series to emulate the inductance of a transmission line. Microinverters number 11 through 20 are conventional GFL inverters, and they are also grouped into two clusters of five units: microinverters 11–15 and microinverters 16–20. Another inductor (L4) is placed between the two clusters of microinverters to emulate the inductance of a transmission line. Each set of 10 microinverters is connected to a series inductor before connecting to a resistive load bank. Microinverters 1–10 connect to the load bank through the inductor L2, which is also a model for a transmission line. Microinverters 11–20 connect to the load bank through the inductor L3. The inductance values are as follows: L1 = 7.7 mH, L2 = 11.6 mH, L3 = 11.6 mH, and L4 = 7.7 mH. Each set of 10 microinverters is sourced by a DC power supply through a DC distribution box, as illustrated in Figure 338.

The resistive load bank was an off-the-shelf portable load bank manufactured by Simplex. The resistive load bank, controlled with toggle switches, allows for load steps of 250 W, 500 W, 1,000 W, and 2,000 W with a maximum load capacity of 10 kW at 240 Vrms. Connected in parallel is a 10-microfarad capacitor through one of the toggle switches in the load bank.

The test bed contains a total of four power line communication modules. As shown in Figure 38, each cluster of five microinverters is equipped with a power line communication module including USB interface to control the test bed operation.

For the user interface, a Python script with several functions was developed. Figure 39 shows a picture of the two cabinets that comprise the 20 microinverter test bed. The contents of each cabinet are noted in Figure 39.

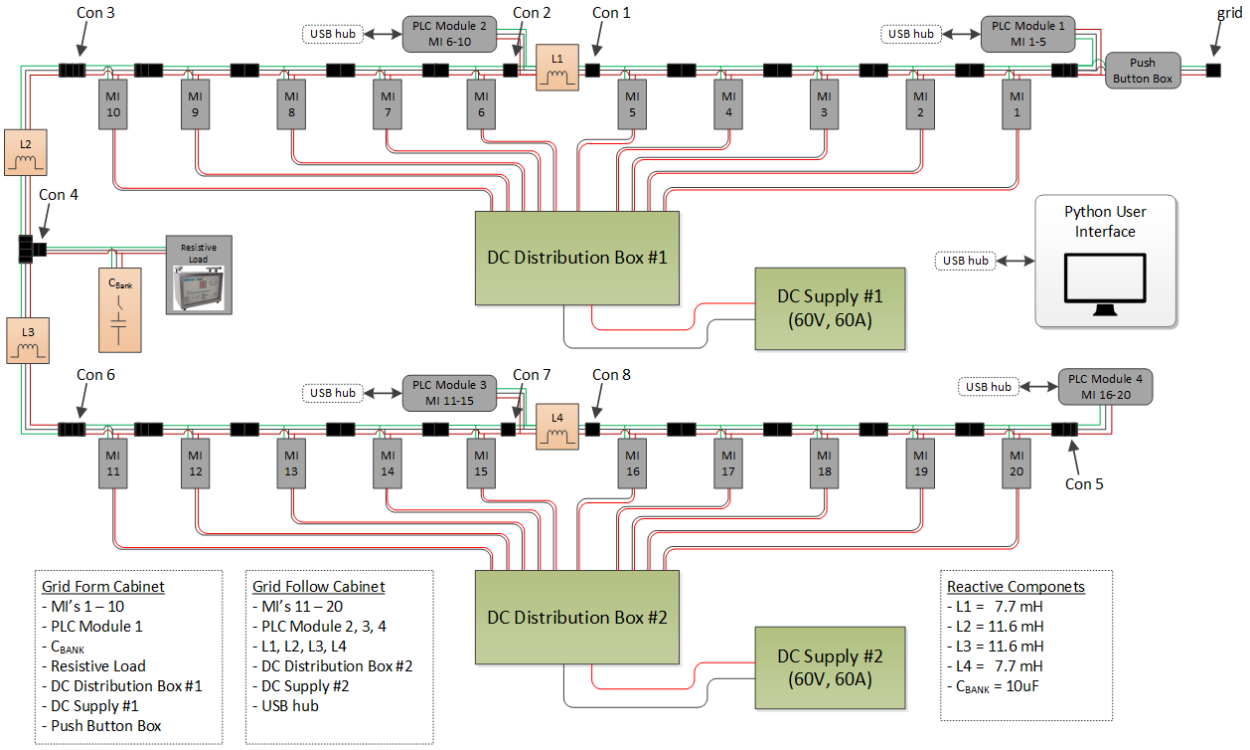

Figure 38. The 20-microinverter test bed electrical diagram: microinverters 1–10 are GFM, and microinverters 11–20 are GFL.

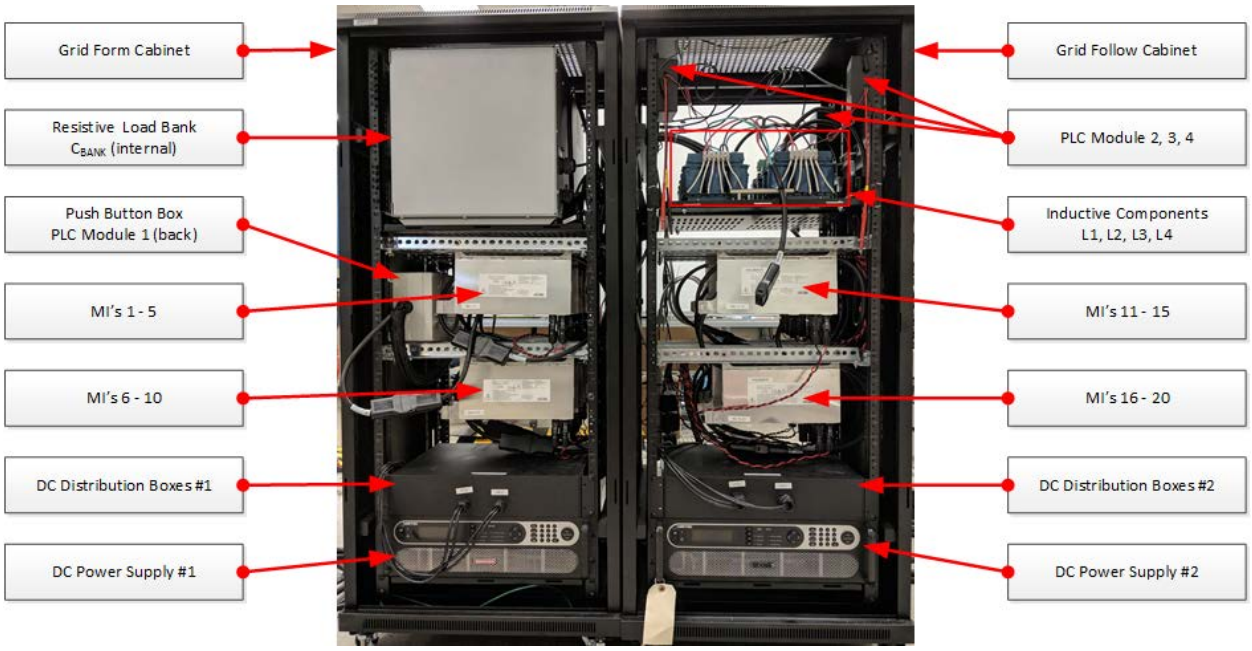

Figure 39. Microinverter test bed: (left) 10-GFM microinverter cabinet and (right) 10-GFL microinverter cabinet. *Photo by NREL*

3.7.2 System Test Sequence and Experimental Results

A test sequence was created and is summarized in Table 9.

Table 9. Twenty-Microinverter Test Bed Experimental Test Sequence

Steps	Description	Load (W)	Capacity (W)	GFM Power (W)	GFL Power (W)
1	Enable microinveters 1–5 as GFM inverters	250	1,280	250	0
2	Increase load (500-W step change)	750	1,280	750	0
3	Enable microinveters 11–15 as GFL inverters (to 100W)	750	1,780	250	500
4	Increase load (1,000-W step change)	1,750	1,780	1,250	500
5	Increase power of microinveters 11–15 from 100 W to 200 W	1,750	2,280	750	1,000
6	Switch in capacitor bank	1,750	2,280	750	1,000
7	Enable microinveters 6–10 as GFM inverters	1,750	3,560	750	1,000
8	Enable microinveters 16–20 as GFL inverters (to 50 W)	1,750	3,560	500	1,250

In Step 1, a first cluster of five GFM microinveters (1–5) is enabled. The load is set to 250 W, and all other microinveters are in a passive state (turned off). Microinverters 1–5 supply and share the 250-W load and the reactive current drawn by the output filters of the passive microinveters (15), as shown in Figure 40. The figure shows load voltage (Channel 4), load current (Channel 3), the current out from Microinveter 1 (Channel 1), and the current through L1. Because the GFM microinveters are turned on one by one from Microinveter 1, Microinveter 1 should black-start under the condition with all other microinveters off. After Microinveter 1 is enabled, the microinveter cannot generate enough current to satisfy the 250-W load and the significant reactive load drawn by the passive microinveter output filters, resulting in a power-limited grid with a reduced voltage of approximately 140 Vrms. Then Microinveter 2 is enabled to join the black-start. The two microinveters can now meet the load demand, which increases the load voltage to approximately 240 Vrms. As the rest of the microinveters (3–5) come online, the grid is collectively maintained by the five microinveters. Note the voltage continues to increase as one inverter comes online because of the droop behavior of the VOC. Channel 1 shows the current from Microinveter 1 decreasing as each microinveter is enabled, which is a result of the microinveters sharing the load demand.

Step 2 is shown in Figure 41, which captures the step change in the load from 250 W to 750 W. At that point, microinveters 1–5 supply all power and must support the step change with minimal disturbance to the system voltage. Channels 4 and 3 show the load voltage and load current, respectively. The load current increases and the load voltage decreases slightly because of the droop behavior of the VOC. Channel 2 is the current through L1, the sum of the currents from microinveters 1–5. They supply all the power to the load in addition to the reactive current to all the passive microinveters. Channel 1 is the current through L3, the sum of the reactive current drawn by the GFL microinveters (11–20).

Step 3, shown in Table 9, enables the cluster of five GFL microinveters (11–15) to produce 100 W each. Figure 42 shows that the load voltage and current (Channel 4 and Channel 3) are unchanged as the GFM microinveters (11–15) are enabled. The figure also shows on Channel 2 the current through L1, the sum of the GFM microinveters (1–5). Initially, the current through L1

supplies the load and all the reactive current drawn by the passive MIs. Then, as microinveters 11–15 are enabled to produce 100 W each, the current through L1 decreases because the effective load seen by the GFM microinveters is decreasing. Channel 1 shows the current through L3, the sum of the currents from microinveters 11–20.

Step 4, shown in Table 8, is a step change in the load from 750 W to 1,750 W. Microinveters 11–15 are programmed to supply 500 W (100 W each) while microinveters 1–5 supply the remaining power to the load to regulate the microgrid. A load step increase of 1,000 W is imposed, and the transient is shown in Figure 43. Channel 3 shows the load current increase after the load change. The load voltage in Channel 4 undergoes a small decrease, which is caused by the droop behavior of the VOC. The current through L3 in Channel 1, which is the current from the GFL microinveters, increases slightly to maintain a 100-W/ microinveter output resulting from voltage decrease. Channel 2 shows the current through L1, the sum of the current from the enabled GFM microinveters (1–5). They adjust their output power to meet the step change demand by the load, causing minimal voltage disturbance.

In Step 5, shown in Table 8, the power generation of the GFL microinveters (11–15) is increased from 100 W to 200 W for each unit, and scope data are captured in Figure 44. Channel 4 and Channel 3 show the load voltage and load current, which remains steady while the microinveters change their power setting. Channel 2 captures the current through L1, the sum of the current from GFM microinveters 1–5. Channel 1 is the current through L3, the sum of the current from the GFL microinveters 11–15. As the GFL microinveters increase output power, the GFM microinveters decrease their output to regulate the grid voltage.

In Step 6, a 10-microfarad capacitor bank connected in parallel to the resistive load is switched into the circuit. Figure 45 shows the system voltage and currents before and after the capacitor bank is involved. Channels 4 and 3 show the load voltage and current. The current through L1 is shown in Channel 2, and the current through L2 is captured in Channel 1. The expected effect of adding a capacitive bank in parallel with the load is to recover some of the voltage drop at the load caused by the inductive elements in the system. The increase can be observed in the load current and current of L1. On the other hand, the current through L3 in Channel 1 reduces slightly to maintain the constant power set point of GFL microinveters 11–15 (constant power generated from following microinveters).

Step 7 shows that the remaining GFM microinveters (6–10) are enabled. The load bank is held constant at 1,750W, and Figure 46 shows a capture of the transition. As before, Channel 4 and Channel 3 capture the load voltage and load current. Channel 2 shows the current through L1, which is decreasing as microinveters 6–10 are enabled (Microinveter 10 was off-screen and not captured). Channel 1 is the current through L2, which remains relatively constant because the amount of power from the GFM inverters remains with the load not changing.

Step 8 captures the operation with all microinveters generating power. Microinveters 16–20 were enabled to a power set point of 50 W each. Figure 47 captures the transition of microinveters 16–20. As expected, the current through L1 and L2 (shown in Ch 2 and Ch 3) decrease as each GFL microinveter is enabled.

In summary, the test bed was designed, assembled, and tested at NREL. Simulation models were used to choose the reactive components and to help design the test sequence. The experimental data showed that the GFM controller can regulate the grid and can be compatible with commercial GFL inverters to form a grid. During the implementation of the test sequences, there were several occurrences where the system would fault and shut down. It was found that some of the shutdowns were caused by the pulse width modulation switching scheme employed by the microinveter. Low-level firmware was adjusted to resolve some of the faults; however, we still identify the system faults under various conditions and steps. It is unclear whether the system fault was caused by the GFM and GFL control compatibility or caused by the microinveter hardware. More investigation should be conducted to fully analyze the issues and to complete the system if we consider deploying GFM controls for renewable energy resources.

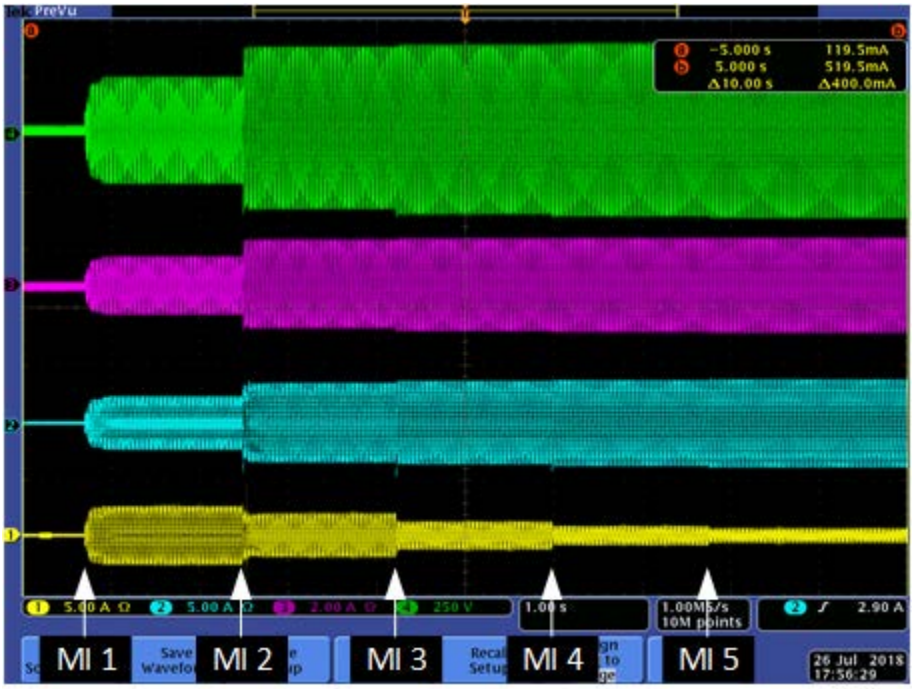

Figure 40. Test sequence Step 1: black-start the grid with microinveters 1–5—Channel 1 is the current from Microinveter 1, Channel 2 is the current through L1, Channel 3 is the load current, and Channel 4 is the load voltage.

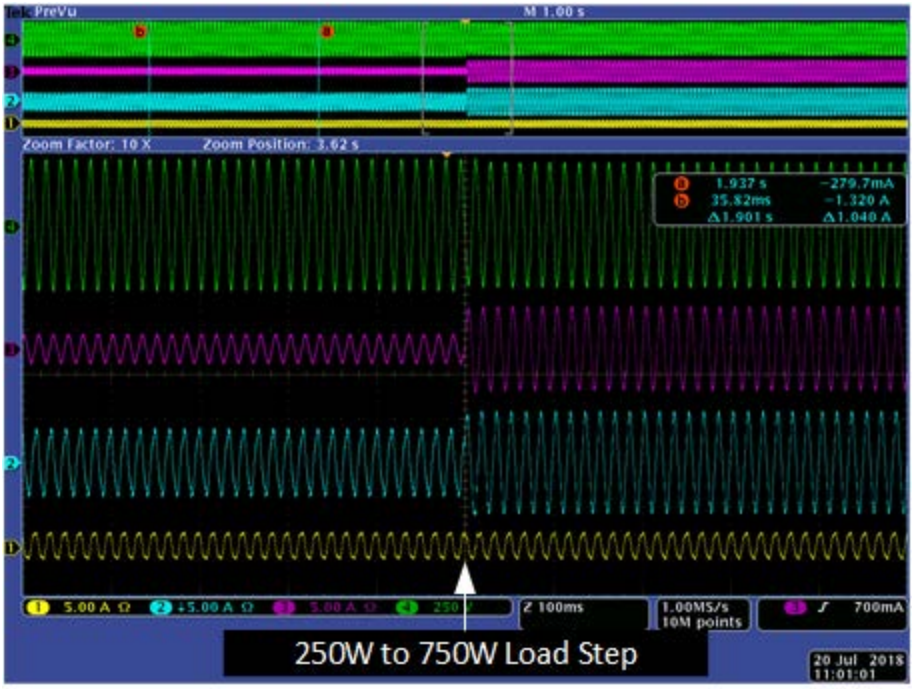

Figure 41. Test sequence Step 2: load step from 250 W to 750 W—Channel 1 is the current through L3, Channel 2 is the current through L1, Channel 3 is the load current, and Channel 4 is the load voltage.

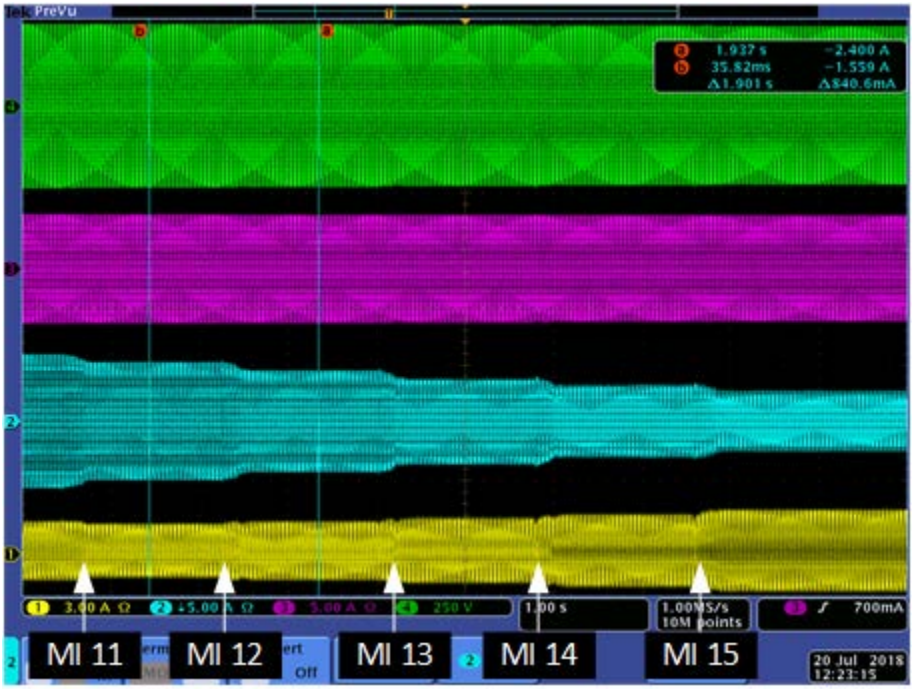

Figure 42. Test sequence Step 3: turning on microinveters 11–15—Channel 1 is the current through L3, Channel 2 is the current through L1, Channel 3 is the load current, and Channel 4 is the load voltage.

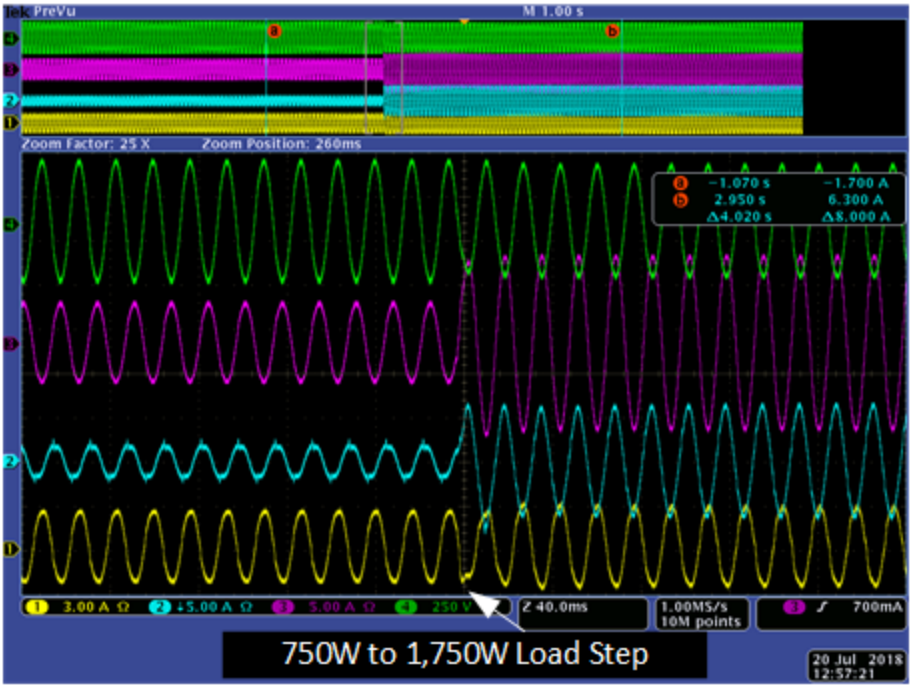

Figure 43. Test sequence Step 4: load change from 750 W to 1,750 W—Channel 1 is the current through L3, Channel 2 is the current through L1, Channel 3 is the load current, and Channel 4 is the load voltage.

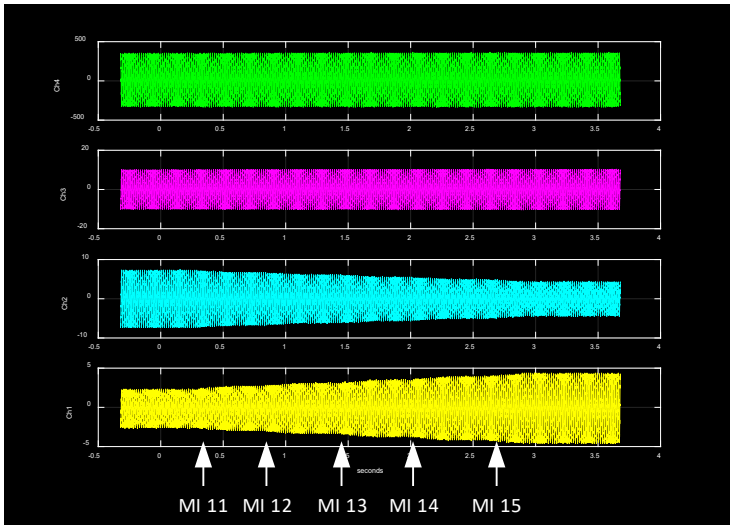

Figure 44. Test sequence Step 5: increasing power generation of microinverters 11–15 from 100 W to 200 W each—Channel 1 is the current through L3, Channel 2 is the current through L1, Channel 3 is the load current, and Channel 4 is the load voltage.

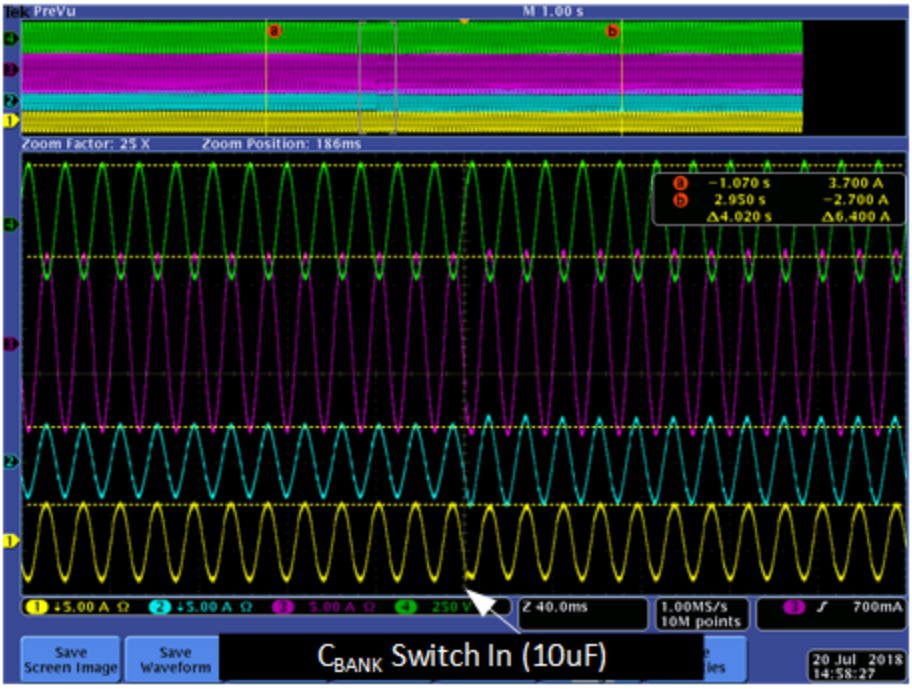

Figure 45. Test sequence Step 6, involving 10-uF capacitor bank—Channel 1 is the current through L3, Channel 2 is the current through L1, Channel 3 is the load current, and Channel 4 is the load voltage.

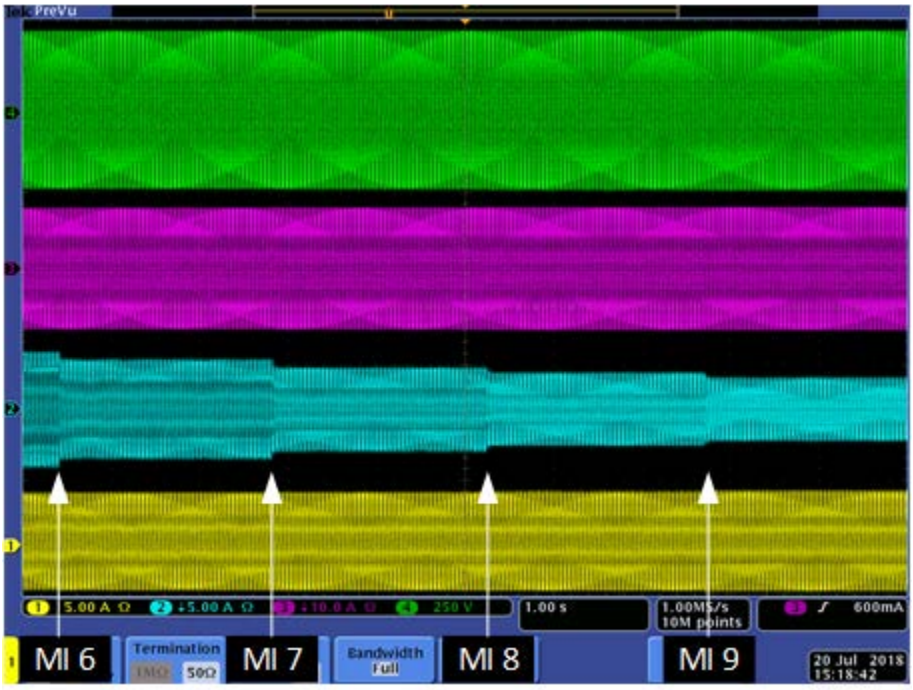

Figure 46. Test sequence Step 7, involving microinveters 11–15 to regulate the system—Channel 1 is the current through L2, Channel 2 is the current through L1, Channel 3 is the load current, and Channel 4 is the load voltage.

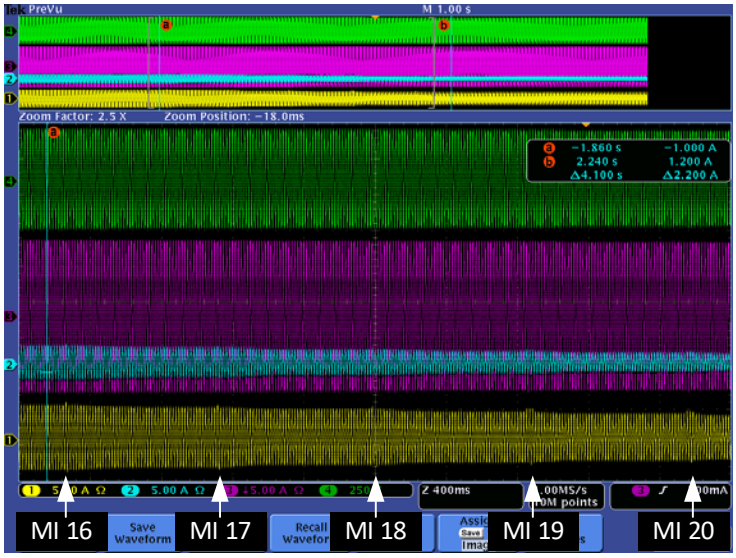

Figure 47. Test sequence Step 8, enabling microinveters 16–20 to generate 50 W each—Channel 1 is the current through L2, Channel 2 is the current through L1, Channel 3 is the load current, and Channel 4 is the load voltage.

3.8 Positive-Sequence Load Flow Simulation

To evaluate the performance of GFM inverters in large-scale systems, the team developed and tested a positive-sequence model of a mixed machine-inverter system in a positive-sequence load flow. Two different systems were studied: one is the modified IEEE 39-bus system, and the other is the microWECC test system developed at Montana Technological University to represent a simplified version of the North American Western Interconnection. Slight modifications to the two systems were implemented to achieve more realistic results.

All generators in the test systems were split into two generators on parallel buses—one conventional generator and one PV generator—except at Bus 30 in the IEEE test system and Bus 12 in the microWECC. Bus 30 and Bus 12 were tripped offline as the contingency simulated throughout this report. It was considered that there is unlimited headroom for the PV, although this is not realistic, but the project goals did not include research on saturation logic; this is a topic of future work.

In both the microWECC and 39-bus system, three different cases were compared:

- A 100% conventional synchronous generation case (5% frequency droop; the voltage droop is left the same as in the original IEEE 39-bus and microWECC models, which is different for each generator)
- 50% PV with the GFM VOC dynamic model (5% frequency droop, 2% voltage droop)
- 50% PV with the GFM droop dynamic model (5% frequency droop, 2% voltage droop).

To compare the dynamics of the three cases in isolation, frequency droop was kept relatively constant across all cases. Originally only the IEEE 39-bus test system was used, but the IEEE 39-bus test system is based on a system in New England. Dynamics in the U.S. Eastern Interconnection typically have a “lazy L” shape (during a generation trip). In this case, there is not a significant frequency nadir compared to the settling frequency. At first, to increase the

frequency nadir, modifications were made to the IEEE 39-bus test system, such as decreasing system inertia, changing the governor time constants, and increasing the proportion of constant power load; however, these changes made the system vastly different than the original.

To investigate the system behavior in a manner more commensurate with the current system, dynamic simulations were also carried out on the microWECC. The U.S. Western Interconnection system typically has a more significant frequency nadir than the U.S. Eastern Interconnection. The microWECC was used to understand the PV model impact on the frequency nadir. Simulations results indicate that the PV controls developed in this project can significantly affect the bulk system frequency behavior, as shown in the next sections. The results are reported in Pierre et. al. (2019).

The primary takeaway from the positive-sequence load flow simulations comparing the synchronous generator case to the two GFM inverter cases is that the dynamic performance of the GFM inverters is very similar to that of conventional synchronous generators. All three cases show similar behavior in frequency/voltage with nearly identical nadirs and steady-state conditions. The simulations indicate that grid stability will not be affected by up to a 50% penetration of PV for either VOC or droop control. Note that because of the time step limitation, the PLL and VOC switching fast dynamics of the inverters are not included in the positive-sequence load flow model. This could lead to some actual behavior in practice not being captured in the simulation.

3.9 Research Road Map on Grid-Forming Inverters

The project team recognizes that there is no established body of experience for operating hybrid power systems with significant amounts of inverter-based resources at the scale of today's North American interconnections; thus, we developed a research road map for GFM inverters, which is intended to provide a comprehensive analysis of the challenges in integrating inverter-based resources and offer recommendations on potential technology pathways to inform the academic community, industry, and government research organizations. Although the focus of this road map is on GFM inverter controls, their impact on grid stability, and evaluating crucial system interactions (e.g., protection), we recognize that the large interconnections in North America will comprise both electromechanical and inverter-based resources (in this road map, sometimes called a hybrid power system). More importantly, we further recognize that inverter-based resources will comprise both GFM resources and other forms of control, such as GFL resources. Transitioning to a grid with more inverter-based resources poses major challenges because the operation of future power systems must be based on a combination of the physical properties and control responses of traditional, large synchronous generators as well as those of numerous and diverse inverter-based resources.

This research road map is intended to fill the knowledge gap by providing a system view of GFM inverter-based resource controls and their impact on grid stability, which we believe is central to meeting some of the challenges to operating the future North American electric power system. This includes the roles and requirements of GFM inverter-based resources—including solar PV, wind generators, and energy storage. Although the road map focuses narrowly on system challenges for GFM controls and power system stability, including interactions with protection, we hope it serves as a foundational element for future system-of-systems road-

mapping needed in a broader grid modernization effort with increasing deployments of inverter-based resources.

The road map first introduces formal definitions for the grid stability topics and then describes the differences between GFM and traditional GFL control approaches for inverter-based resources. The core of the road map consists of a review of current research and an outline of research needs related to five GFM inverter topics:

- Frequency control
- Voltage control
- System protection
- Fault ride-through and voltage recovery
- Modeling and simulation.

The review both delineates contemporary advances and highlights open research questions that must be addressed to enable the widespread adoption of inverter-based resources across the grid. Feedback from industry on these research questions is incorporated, including discussions during the Workshop on Grid-Forming Inverters for Low-Inertia Power Systems.[3] The workshop included industry presentations and discussion of ongoing research, technology gaps, and piloting needs.

This road map concludes by offering a multiyear perspective on the gradual field validation of GFM inverters (see Figure 48). This perspective recognizes that the scale and scope of the types of power systems that inverters will be called on to provide GFM services will and should begin modestly. Specifically, this road map recognizes that inverter controls today are predominantly GFL and that future power systems will involve a mix of inverter-based resources with both GFL and GFM control capabilities. Growth over time will depend on how well GFM inverters perform and what advantages they bring as penetration levels (instantaneous and average) of inverter-based resources increases. This recognition, in turn, establishes a natural sequence of priorities for the research questions that must be addressed.

[3] The Workshop on Grid-Forming Inverters for Low-Inertia Power Systems was held at the University of Washington in Seattle on April 29–30 2019. Presentations and video are available at https://lowinertiagrids.ece.uw.edu/.

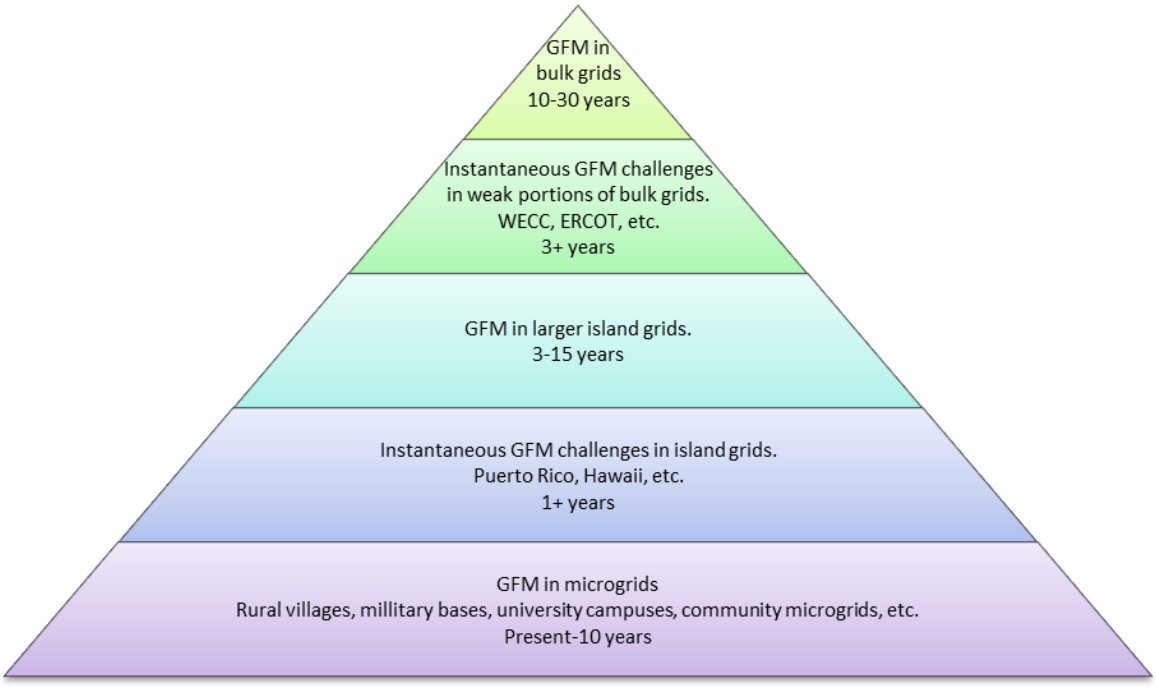

Figure 48. Incorporating GFM controls into the electric grid will take place gradually after key functionalities have been demonstrated and confidence has been gained by operating them in smaller microgrids and island power systems.

Following this multiyear perspective, the road map offers short descriptions of two specific near-term research priorities: the review of regulatory and technical standards and the development of advanced modeling techniques. These priorities are foundational. We recommend immediate pursuit of them in parallel with and in direct support of the research outlined by our multiyear perspective.

4 Significant Accomplishments and Conclusions

During the project, the team made advances in the diverse domains of fundamental mathematical analysis, control development and validation, and enhancing U.S. Department of Energy (DOE) laboratory visibility. Specifically, our team made significant progress with respect to the development of analytical models for traditional GFL inverter systems, novel GFM controllers that are compatible with existing practice, a flexible simulation-to-experimentation test bed that allows for rapid prototyping, custom hardware, new intellectual property, and multiple publications. The team also created a research road map for GFM inverters that outlines the state of the art and future research directions.

The major accomplishments of the project include:

- We developed a comprehensive modeling framework and accompanying case studies for the stability assessment of low-inertia grids with significant penetrations of inverter-based resources. The case studies considered both the business-as-usual GFL inverter control and the new GFM inverter control. Results show that the system could become unstable as the inverter penetration level increases, and this tipping point depends on several system parameters (such as inverter controller gains and filter parameters). Results also show that GFM inverters can potentially improve the stability of the system.
- We designed, analyzed, and validated a next-generation GFM inverter controller, the VOC. We demonstrated that the new controller can regulate inverter output voltage without external voltage reference, can share load autonomously among multiple inverters, and is compatible with existing power grid.
- We created a research road map on GFM inverters (Lin et. al. 2020). The document outlines specific research directions appropriate for inclusion in an eventual U.S. national research-and-development program on GFM inverter-based generation and storage that can enhance the stability of the future electric power system.

5 Inventions, Patents, Publications, and Other Results

Technical Report

- Lin, Y., J. H. Eto, B. B. Johnson, J. D. Flicker, R. H. Lasseter, H. N. Villegas Pico, G. S. Seo, B. J. Pierre, and A. Ellis. *Research Roadmap on Grid-Forming Inverters* (NREL/TP-5D00-73476). Golden, CO: National Renewable Energy Laboratory, 2020.

Patents

- Johnson, B., S. Dhople, A. Hamadeh, and P. Krein. Virtual Oscillator Control of Power Electronics Inverters. U.S. Patent 9,484,745. 2016.
- Johnson, B., M. Rodriguez, S. Dhople, and M. Sinha. Communication Free Interleaving for Distortion Cancellation. Submitted 2017. Application Number 62/502,215.
- Johnson, B., D. Maksimovic, and P. Achanta. Modular Scalable Power Conversion. Submitted 2017. Application Number 62/516,316.

Journal papers

- Achanta, P. K., B. B. Johnson, G. S. Seo, and D. Maksimovic. "A Multilevel DC to Three-Phase AC Architecture for Photovoltaic Power Plants." *IEEE Transactions on Energy Conversion*, 34, no. 1 (2019): 181–90.
- Pico, H. N. V., and B. B. Johnson. "Transient Stability Assessment of Multi-Machine Multi-Converter Power Systems." *IEEE Transactions on Power Systems* 34, no. 5 (2019): 3,504–14.
- Purba, V., B. B. Johnson, M. Rodriguez, S. Jafarpour, F. Bullo, and S. Dhople. "Reduced-Order Aggregate Model for Parallel-Connected Single-Phase Inverters." *IEEE Transactions on Energy Conversion* 34, no. 2 (2018): 824–37.
- Kroposki, B., B. Johnson, Y. Zhang, V. Gevorgian, P. Denholm, B. M. Hodge, and B. Hannegan. "Achieving a 100% Renewable Grid: Operating Electric Power Systems with Extremely High Levels of Variable Renewable Energy." *IEEE Power and Energy Magazine* 15, no. 2 (2017): 61–73.
- Johnson, B. B., M. Sinha, N. G. Ainsworth, F. Dörfler, and S. V. Dhople. "Synthesizing Virtual Oscillators to Control Islanded Inverters." *IEEE Transactions on Power Electronics* 31, no. 8 (2015): 6002–15.
- Sinha, M., F. Dörfler, B. B. Johnson, and S. V. Dhople. "Uncovering Droop Control Laws Embedded within the Nonlinear Dynamics of Van der Pol Oscillators." *IEEE Transactions on Control of Network Systems* 4, no. 2 (2015): 347–58.

Conference papers:

- Pierre, B. J., H. N. V. Pico, R. T. Elliott, J. Flicker, Y. Lin, B. B. Johnson, J. H. Eto, Lasseter, and A. Ellis. "Bulk Power System Dynamics with Varying Levels of Synchronous Generators and Grid-Forming Power Inverters." In *2019 IEEE 46th Photovoltaic Specialists Conference (PVSC)* (June 2019): 0880–0886.

- Seo, G. S., M. Colombino, L. Subotic, B. Johnson, D. Groß, and F. Dörfler. "Dispatchable Virtual Oscillator Control for Decentralized Inverter-Dominated Power Systems: Analysis and Experiments." In *2019 IEEE Applied Power Electronics Conference and Exposition (APEC)* (March 2019): 561–566.
- Khan, M. M. S., Y. Lin, B. Johnson, M. Sinha, and S. Dhople. "Stability Assessment of a System Comprising a Single Machine and a Virtual Oscillator Controlled Inverter with Scalable Ratings." In *IECON 2018-44th Annual Conference of the IEEE Industrial Electronics Society* (October 2018): 4057–62.
- Liu, Z., Z. Zhang, and Y. Lin. "Impact of Inverter-Interfaced Renewable Generation on Transient Stability at Varying Levels of Penetration." In *IECON 2018-44th Annual Conference of the IEEE Industrial Electronics Society* (October 2018): 4027–32.
- Achanta, P., M. Sinha, B. Johnson, S. Dhople, and D. Maksimovic. "Self-Synchronizing Series-Connected Inverters." In *2018 IEEE 19th Workshop on Control and Modeling for Power Electronics (COMPEL)* (June 2018): 1–6.
- Khan, M. M. S., Y. Lin, B. Johnson, V. Purba, M. Sinha, and S. Dhople. "A Reduced-Order Aggregated Model for Parallel Inverter Systems with Virtual Oscillator Control." In *2018 IEEE 19th Workshop on Control and Modeling for Power Electronics (COMPEL)* (June 2018): 1–6.
- Poon, J., B. B. Johnson, S. V. Dhople, and S. R. Sanders. "Minimum Distortion Point Tracking: Optimal Phase Shifting for Input-or Output-Parallel Connected DC-DC Converters." In *2018 IEEE 19th Workshop on Control and Modeling for Power Electronics (COMPEL)* (June 2018): 1–6.
- Achanta, P., D. Maksimovic, and B. Johnson. "Cascaded Quadruple Active Bridge Structures for Multilevel DC to Three-Phase AC Conversion." In *2018 IEEE Applied Power Electronics Conference and Exposition (APEC)* (March 2018): 156–60.
- Purba, V., S. V. Dhople, S. Jafarpour, F. Bullo, and B. B. Johnson. "Network-Cognizant Model Reduction of Grid-Tied Three-Phase Inverters." In *2017 55th Annual Allerton Conference on Communication, Control, and Computing (Allerton)* (October 2017): 157–64.
- Lin, Y., B. Johnson, V. Gevorgian, V. Purba, and S. Dhople. "Stability Assessment of a System Comprising a Single Machine and Inverter with Scalable Ratings." In *2017 North American Power Symposium (NAPS)* (September 2017): 1–6.
- Johnson, B., M. Rodriguez, M. Sinha, and S. Dhople. "Comparison of Virtual Oscillator and Droop Control." In *2017 IEEE 18th Workshop on Control and Modeling for Power Electronics (COMPEL)* (July 2017): 1–6.
- Purba, V., S. V. Dhople, S. Jafarpour, F. Bullo, and B. B. Johnson. "Reduced-Order Structure-Preserving Model for Parallel-Connected Three-Phase Grid-Tied Inverters." In *2017 IEEE 18th Workshop on Control and Modeling for Power Electronics (COMPEL)* (July 2017): 1–7.
- Sinha, M., S. Dhople, B. Johnson, M. Rodriguez, and J. Poon. "Decentralized Interleaving of Paralleled DC-DC Buck Converters." In *2017 IEEE 18th Workshop on Control and Modeling for Power Electronics (COMPEL)* (July 2017): 1–6.

6 Path Forward

As an emerging topic, the development of GFM inverters is still in its early stage. The team created a research road map for GFM inverters (Lin et. al. 2020) that outlines specific research directions appropriate for inclusion in an eventual U.S. national research-and-development program on GFM inverter-based forms of generation that can enhance the stability of the future electric power system. The report also highlights the priorities for research needed during the coming 5–10 years. Key issues that need to be addressed include protection, modeling and simulation tools, and standard development. The interested reader can refer to the full road map for more detailed discussion.

References

Alatrash, H., A. Mensah, E. Mark, G. Haddad, and J. Enslin. 2012. "Generator Emulation Controls for Photovoltaic Inverters." *IEEE Transactions on Smart Grid* 3 (2): 996–1,011.

Beck, H. P., and R. Hesse. 2007. "Virtual Synchronous Machine." *9th International Conference on Electrical Power Quality and Utilisation*, Barcelona, Spain, October 9–11, 2007, 1–6.

Bergen, A. R., and D. J. Hill. 1981. "A Structure Preserving Model for Power System Stability Analysis." *IEEE Transactions on Power Apparatus and Systems* (1): 25–35.

Chandorkar, M. C., D. M. Divan, and R. Adapa. 1993. "Control of Parallel Connected Inverters in Standalone AC Supply Systems." *IEEE Transactions on Industry Applications* 29 (1): 136–43.

Dong, D., B. Wen, D. Boroyevich, P. Mattavelli, and Y. Xue. 2014. "Analysis of Phase-Locked Loop Low-Frequency Stability in Three-Phase Grid-Connected Power Converters Considering Impedance Interactions." *IEEE Transactions on Industrial Electronics* 62 (1): 310–21.

Guerrero, J. M., L. G. De Vicuna, J. Matas, M. Castilla, and J. Miret. 2004. "A Wireless Controller to Enhance Dynamic Performance of Parallel Inverters in Distributed Generation Systems." *IEEE Transactions on Power Electronics* 19 (5): 1,205–13.

Johnson, B. B., M. Sinha, N. G. Ainsworth, F. Dörfler, and S. V. Dhople. 2015. "Synthesizing Virtual Oscillators to Control Islanded Inverters." *IEEE Transactions on Power Electronics* 31 (8): 6,002–15.

Johnson, B., M. Rodriguez, M. Sinha, and S. Dhople. 2017. "Comparison of Virtual Oscillator and Droop Control." *2017 IEEE 18th Workshop on Control and Modeling for Power Electronics (COMPEL)*, Stanford, California, July 9–12, 2017, 1–6.

Katiraei, F., M. R. Iravani, and P. W. Lehn. 2007. "Small-Signal Dynamic Model of a Micro-Grid Including Conventional and Electronically Interfaced Distributed Resources." *IET Generation, Transmission & Distribution* 1 (3): 369–78.

Khan, M. M. S., Y. Lin, B. Johnson, M. Sinha, and S. Dhople. 2018a. "Stability Assessment of a System Comprising a Single Machine and a Virtual Oscillator Controlled Inverter with Scalable Ratings. *IECON 2018-44th Annual Conference of the IEEE Industrial Electronics Society*, Washington, D.C., October 21–23, 2018, 4,057–62.

Khan, M. M. S., Y. Lin, B. Johnson, V. Purba, M. Sinha, and S. Dhople. 2018b. "A Reduced-Order Aggregated Model for Parallel Inverter Systems with Virtual Oscillator Control." *2018 IEEE 19th Workshop on Control and Modeling for Power Electronics (COMPEL)*, Padova, Italy, June 25–28, 2018, 1–6.

Kundur, P., N. J. Balu, and M. G. Lauby. 1994. *Power System Stability and Control* (Vol. 7). New York: McGraw-Hill.

Lin, Y., B. Johnson, V. Gevorgian, V. Purba, and S. Dhople. 2017. "Stability Assessment of a System Comprising a Single Machine and Inverter with Scalable Ratings." *2017 North American Power Symposium (NAPS)*, Morgantown, West Virginia, September 17–19, 2017, 1–6.

Lin, Y., J. H. Eto, B. B. Johnson, J. D. Flicker, R. H. Lasseter, H. N. Villegas Pico, G. S. Seo, B. J. Pierre, and A. Ellis. 2020. *Research Roadmap on Grid-Forming Inverters* (NREL/TP-5D00-73476). Golden, CO: National Renewable Energy Laboratory.

Miller, N. W., B. Leonardi, R. D'Aquila, and K. Clark. 2015. *Western Wind and Solar Integration Study Phase 3A: Low Levels of Synchronous Generation* (NREL/TP-5D00-64822). Golden, CO: National Renewable Energy Laboratory.

North American Electric Reliability Corporation (NERC). 2018. *Reliability Guideline: BPS-Connected Inverter-Based Resource Performance*. Atlanta, GA.

Pico, H. N. V., and B. B. Johnson. 2019. "Transient Stability Assessment of Multi-Machine multi-Converter Power Systems." *IEEE Transactions on Power Systems* 34 (5): 3,504–14.

Pierre, B. J., H. N. V. Pico, R. T. Elliott, J. Flicker, Y. Lin, B. B. Johnson, J. H. Eto, R. H. Lasseter, and A. Ellis. 2019. "Bulk Power System Dynamics with Varying Levels of Synchronous Generators and Grid-Forming Power Inverters." *2019 IEEE 46th Photovoltaic Specialists Conference (PVSC)*, Chicago, Illinois, June 16–21, 2019, 0880–86.

Pogaku, N., M. Prodanovic, and T. C. Green. 2007. "Modeling, Analysis and Testing of Autonomous Operation of an Inverter-Based Microgrid." *IEEE Transactions on Power Electronics* 22 (2): 613–25.

Purba, V., B. B. Johnson, M. Rodriguez, S. Jafarpour, F. Bullo, and S. V. Dhople. 2018. "Reduced-Order Aggregate Model for Parallel-Connected Single-Phase Inverters." *IEEE Transactions on Energy Conversion* 34 (2): 824–37.

Purba, V., S. V. Dhople, S. Jafarpour, F. Bullo, and B. B. Johnson. 2017. "Reduced-Order Structure-Preserving Model for Parallel-Connected Three-Phase Grid-Tied Inverters." *2017 IEEE 18th Workshop on Control and Modeling for Power Electronics (COMPEL)*, Stanford, California, July 9–12, 2017, 1–7.

Rasheduzzaman, M., J. A. Mueller, and J. W. Kimball. 2015. "Reduced-Order Small-Signal Model of Microgrid Systems." *IEEE Transactions on Sustainable Energy* 6 (4): 1,292–1305.

Simpson-Porco, J. W., F. Dörfler, and F. Bullo. 2013. "Synchronization and Power Sharing for Droop-Controlled Inverters in Islanded Microgrids." *Automatica* 49 (9): 2,603–11.

Sinha, M., F. Dörfler, B. B. Johnson, and S. V. Dhople. 2015a. "Uncovering Droop Control Laws Embedded Within the Nonlinear Dynamics of Van der Pol Oscillators." *IEEE Transactions on Control of Network Systems* 4 (2): 347–58.

Zhong, Q. C. 2016. "Virtual Synchronous Machines: A Unified Interface for Grid Integration." *IEEE Power Electronics Magazine* 3 (4): 18–27.